Non-equilibrium fluid-wall interaction in high-Mach regimes

Marie-Eve Dumas

Department of Mechanical Engineering

McGill University

Montréal, Québec

April 2017

A Thesis Submitted to McGill University in

Partial Fulfillment of the Requirements of the Degree of Master of Engineering

Abstract

Futuristic civil airliners will fly at much higher speeds than current commercial fleets, and at altitudes where the atmospheric density and the residence time of fluid particles are greatly reduced. Under such flight conditions, the continuum hypothesis of the Navier-Stokes equations may become invalid due to local non-equilibrium. It manifests itself at the solid-gas interface as a jump in flow variables at the vehicle's surface, with both velocity and temperature of the flow not matching their wall values. Numerical velocity and temperature gradients at solid surfaces would be inaccurate for aerothermodynamic calculations.

The current work presents the development of a Consistent Galerkin approach to impose slip/jump boundary conditions based on the Weighted Residual method. The weak-Galerkin forms of the energy and momentum equations are solved to yield the heat flux and shear stress of the wall nodes to second order accuracy, while maintaining the computational cost remarkably small. This methodology allows extending the validity of the Navier-Stokes equations up to transitional flows.

The methodology is validated in 2D and 3D for flow conditions ranging from quasi-equilibrium to non-equilibrium. A systematic grid refinement analysis is also performed to verify the higher order of accuracy of the proposed methodology.

Résumé

Les avions de ligne du futur voleront à des vitesses grandement supérieures à celles atteintes par les aéronefs commerciaux d'aujourd'hui, ainsi qu'à des altitudes où la densité atmosphérique et le temps de résidence des particules sont fortement réduits. Sous de telles conditions, l'hypothèse de continuité des équations de Navier-Stokes devient invalide dû à la présence d'un non-équilibre local. Celui-ci se manifeste, entre autre, en tant qu'un saut des valeurs de vitesse et de température entre le fluide et les parois du véhicule. La précision des gradients de température et de vitesse aux parois est donc à un niveau insuffisant pour les calculs aérothermodynamiques.

Nous présentons dans cette thèse une approche dite « Consistent Galerkin » en anglais, fondée sur la méthode des résidus pondérés pour imposer le saut de température et de vitesse comme conditions frontières. L'équation de bilan de l'énergie et les équations de bilan de la quantité de mouvement sont résoutes sous la forme Galerkine-faible pour obtenir le cisaillement et le flux thermique à une haute précision, tout en maintenant les coûts de calcul remarquablement bas. Cette méthodologie permet de prolonger la validité des équations de Navier-Stokes aux régimes transitionnels.

La méthodologie est validée à l'aide de problèmes bidimensionnels et tridimensionnels dans des conditions variant du quasi-équilibre au non-équilibre. Une analyse systématique de raffinement du maillage est effectuée et illustre le degré de précision supérieur de la méthodologie proposée.

Acknowledgements

First and foremost, I would like to thank my thesis supervisor Prof. Habashi for the opportunity to participate in cutting edge research at McGill University's CFD Laboratory. I am grateful for his support and guidance. I also extend my gratitude to Dr. Marco Fossati for his direction and assistance with my research. Their advice always gave me the motivation to push the research forward.

I am extremely thankful to Dr. Dario Isola for his constant advices and suggestions and for always being a source of solutions when I encountered difficulties. Additionally, I am grateful to Dr. Guido Baruzzi for his suggestions and review of my research.

I am thankful for my colleagues at the CFD lab: Munir, Jory, Vahid, Ahmed, Song, Wenbo, Zhao, for helping create a positive and supportive environment. Je tiens également à remercier mes amis et ma famille pour votre support, vos encouragements et votre compréhension.

I would also like to thank the NSERC-Lockheed Martin-Bell Helicopter Industrial Research Chair whose generous financial support permitted this work. I am grateful to Compute Canada and CLUMEQ as well for the access to their computing resources that facilitated this work

Lastly, Stef. Thank you. You make everything better.

Table of Contents

Nomenclature

Abbreviations

CFD	Computational fluid dynamics
DSMC	Direct Simulation Monte Carlo
HALO3D	High-Altitude Low-Orbit
LeMANS	(Le) Michigan Aerothermodynamic Navier-Stokes
N-S	Navier-Stokes
RANS	Reynolds-Averaged Navier-Stokes
TPS	Thermal protection system

Greek Symbols

μ_B	Bulk viscosity
ρ	Density
σ^*	Differential cross-section
Θ	Differential solid angle
μ	Dynamic viscosity
λ	Mean free path
η	Second viscosity coefficient
τ	Shear stress
γ	Specific heat ratio

Ω	Tessalation of the domain

Roman Symbols

K	Boltzmann's constant
l	Characteristic length
Q	Conservative state vector
F^B	External forces
N_j	FEM shape function at node *j*
R	Gas constant
q	Heat flux
$\mathcal{F}_i$	Inviscid flux
Kn	Knudsen number
M	Mach number
n	Number density
N	Number of nodes
$c^{*}{}'$	Post-collision velocity of particles
Pr	Prandtl number
P	Pressure
Re	Reynolds number
$H^1(\Omega)$	Sobolev space
T	Temperature
k	Thermal conductivity coefficient

$\mathcal{F}_T$	Thermal flux
E	Total energy per mass
$\mathcal{F}_T$	Thermal flux
h	Total enthalpy
V	Velocity
$\mathcal{F}_v$	Viscous flux
w	Wall
W_i	Weight functions

List of Figures

List of Tables

Chapter 1 Introduction

1.1 Motivation

Futuristic civil airliners will fly at speeds and altitudes much higher than current commercial fleets [1] in conditions ranging from continuum to free molecular flow [2] and under conditions where a thin shock and entropy layer, high temperature effects and viscous interaction form a complex scenario affecting the performance and controllability of the vehicle [3, 4].

To ensure the safety of space transportation, the Federal Aviation Administration (FAA) has issued a regulation system (FAR) addressing safety factors for reusable launch and re-entry vehicles [5, 6]. One aspect of the certification focuses on hazard identification. The Preliminary Hazard Analysis (PHA) as recommended by the Federal Aviation Regulation (FAR), lists multiple safety vulnerabilities helping identify possible risks for space missions.

Based on the PHA, a study examining 99 mishaps in hypersonic flights identified that heat protection issue represents 87% of all protective system failures [7] highlighting the need for a better understanding and modeling of physical processes. Moreover, following the crash of the US Defense Advanced Research Projects Agency (DARPA) HTV-2, the Engineering Review Board (ERB), from its investigation of the accident, noted that [8]:

"[…] a gradual wearing away of the vehicle's skin as it reached stress tolerance limits was expected. However, larger than anticipated portions of the vehicle's skin peeled from the aerostructure."

Further concluding that [9]:

" […] extrapolating from known flight regimes and relying solely on advanced thermal modeling and ground testing could not successfully predict the harsh realities of Mach 20 atmospheric flight."

Proper understanding of the underlying physics is vital to the conception and design of re-entry vehicles [1, 4]. The key challenge to mitigate risk factors is therefore to understand these new flight dynamics [7].

1.2 Wind Tunnel Testing and Flight Testing in the Hypersonic Regime

The current certification and design processes rely on numerical simulations (CFD), ground based facilities / wind tunnels and flight testing [10]. With the increasing power of computers and software, wind tunnels are more and more used as a validation tool for numerical modeling [11] due to the high cost and technical complexity associated with hypersonic testing. As wind tunnel simulations are performed on reduced-model, in order to retain the physics of the full scaled problem, the same Reynolds and Mach number as the full-scale problem must be maintained, requiring reduction in the viscosity and / or an increase in the density to compensate for the undersized model [11]. Given the large range of Mach and Reynolds numbers a hypersonic vehicle

encounters [12], it often requires a specialized facility to model each regime [11]. Furthermore, the extreme temperatures and pressures necessary to accurately reproduce hypersonic / rarefied conditions pose a serious limitation to the use of wind tunnel for design and certification [13].

As with ground-based facilities, the cost and risk of flight-testing is prohibitive and similarly, not all hypersonic flight conditions can be replicated during the limited number of runs. Nonetheless, flight testing remains necessary as it provides information that wind tunnels and CFD cannot, especially for boundary layer transition (BLT) research [3]. Indeed, the noise being generated from the turbulent boundary layer reflects on the walls of the facility distorting the data. Quiet tunnels have been developed but are often not long enough to model the transition region [3, 14]. Yet, when transition occurs, the boundary layer turbulence can increase the surface heating by five compared to the laminar levels; drastically affecting the choice of thermal protective system (TPS) of the vehicle [3]. Proper modeling of the BLT is therefore crucial.

These technical challenges and limitations force an integrated and coordinated usage of CFD, wind tunnels and flight testing [11, 13] using ground-based facilities and flight-testing as benchmark against which CFD can be validated.

1.3 CFD in Hypersonics

Accurate numerical simulation of hypersonic flows is essential, given the fundamental role of CFD in the design of high-speed aircraft and the high costs and known limits of hypersonic wind tunnels [15, 16]. The numerical study of high-Mach

high-altitude flows requires the modeling of non-equilibrium conditions dictated by the small residence times of fluid dynamics and the reduced molecular collision frequencies. A critical phenomenon that needs to be addressed is the breakdown of the local equilibrium assumption. The validity of the Navier-Stokes (N-S) equations is based on the hypothesis that the gas is in thermodynamic equilibrium, which is true when the frequency of molecular collisions is sufficiently high compared to the typical residence time of a fluid particle. At high altitude, or in strongly rarefied flows, the density, and therefore the number of molecules per unit volume is low and thus the collision frequency is reduced. A similar non-equilibrium condition is observed in regions where large gradients of bulk quantities coexist with the very small residence times caused by very high speeds. In both cases, departure from equilibrium is significant, and when interacting with aircraft surfaces, the fluid slips (velocity slip) over the surface and the temperature of the fluid in contact with the wall does not match the temperature of the body (temperature jump) [1].

Numerically, in high-speed simulations only first order accuracy can be realistically obtained due to the approximations required to capture shocks and other discontinuities [17]. Furthermore, slip conditions require the evaluation of gradients, which are generally only first-order accurate and thus inadequate for aerodynamic design. An approach that can guarantee second order accuracy is therefore needed. A second order accurate Finite Element approach known as the “Consistent-Galerkin Finite Element Method” for the numerical computation of wall shear stresses and heat fluxes is proposed for the slip and jump boundary conditions [18, 19].

1.4 Scope of Current Work

The objective of this thesis is to formulate an optimized FE-based approach to improve the modeling of the non-equilibrium physics in the vicinity of the surface of the vehicle by addressing flows in the slip / transitional regime ($0.01 < Kn < 1$). More generally, the thesis aims to advance the modeling of high-speed non-equilibrium flows to provide the accuracy required to address the challenges of hypersonic aerothermodynamics design.

In this regard, the focus of this research is on these axes:

1. Propose an approach to model non-equilibrium at the wall.
2. Provide a methodology to improve the prediction of surface properties.
3. Study the effects of non-equilibrium on the surface properties of blunt bodies.
4. Study different flow regimes, from the continuum and into the transitional regime.

The content of the dissertation is as follows:

In chapter 2, the concepts of non-equilibrium gas dynamics and the governing equations describing non-equilibrium flows are presented. Chapter 3 presents the formulation of the Maxwell boundary condition for slip velocity and the Smoluchowski formulation for the temperature jump. In chapter 4, the Consistent Galerkin approach to shear stress and heat flux is presented and a systematic grid refinement analysis is performed to verify the order of accuracy of the proposed methodology. Chapters 5 and

6 provide examples of flows in the regime $0.01 < Kn < 1$ to assess the approach. The thesis concludes in chapter 7 with remarks and proposals for future work.

Chapter 2 Simulation of Hypersonic Flows

In this chapter, the fundamentals of hypersonic flow simulation are outlined. Some background on the kinetic theory of gases is provided, specifically, on the behavior of molecules in high-Mach / rarefied regimes. Then, the focus will be on the two main governing equations pertaining to hypersonic gas flow, which are the Boltzmann equation, valid for all regimes, and the N-S equations, valid under the assumption of local quasi-equilibrium. This chapter ends with a discussion of the two numerical methods associated to these equations.

2.1 Non-Equilibrium / Continuum Breakdown

When a gas is in thermodynamic equilibrium there is no net macroscopic flow of matters or energy, and if any changes occur, the flow adjusts instantly. Conversely, when a gas is in non-equilibrium, there are transport of mass, momentum and energy that arise from gradients of species concentration, gradients of velocity and gradients of temperature. The gas returns to equilibrium through intermolecular collisions where the number of collisions required depends on the number of molecules per unit volume and the speed at which the gradients are established.

In practice, flows in equilibrium have a relaxation time sufficiently small, or, inversely, collisional rates sufficiently fast for equilibrium to occur through collisions. In other words, if τ_c is the relaxation time; the time required for the gas to return to equilibrium and if τ_f is the residence time of a particle, that is the time it takes for a

particle to flow past a body, equilibrium requires $\tau_f >> \tau_c$. A gas is said to be in non-equilibrium for all other cases [1, 20].

On the molecular level, the main causes of non-equilibrium are:

1. Short residence times
2. Increased relaxation time

These conditions are encountered in high-Mach / rarefied regimes where, in low-density environment, the mean free path is large and the collision frequency decreases, thus increasing the required relaxation time. In addition, the large gradients present in shock waves and boundary layers reduce the residence time of particles.

The degree of non-equilibrium is measured by the Knudsen number (Kn), defined as the ratio between the mean-free-path of the molecules of the gas (λ) and a characteristic length of the aircraft (l) [21, 22].

$$Kn = \frac{\lambda}{l} \tag{2.1}$$

Typically four different flow regimes can be identified according to the Knudsen number. For Kn < 0.01, the continuum hypothesis holds true and the flow can be appropriately described by the Reynolds-Averaged Navier-Stokes equations (RANS). For Kn between 0.01 and 0.1, the so-called slip regime, non-equilibrium effects become more relevant, especially in the proximity of walls and across shock wave fronts. The fluid can still be analyzed using the N-S equations, but more complex wall boundary conditions are needed to account for the non-equilibrium effects. For Knudsen numbers between 0.1 and 10, the flow is said to be in the transitional regime, where the

thermodynamic assumption of the N-S equations begins to break down and non-equilibrium effects become predominant. Finally, for Kn > 10, the flow is considered to be in the free-molecular regime for which simulation by particle-based techniques is required [23].

2.2 Governing Equations

In this section, the Boltzmann and N-S equations are described, as well as some of their advantages and limitations.

2.2.1 Boltzmann Equation

Consider a function $f^* = f^*(\mathbf{x}^*, \mathbf{c}^*, \mathbf{t}^*)$ that describes the state of a dilute gas with $f^* d^3x^* d^3c^*$ being the expected number of particle in the infinitesimal element $d^3\mathrm{x}^*$, within a velocity in the range $d^3\mathrm{c}^*$ about c^* at time t^* [20, 24]. In the absence of body forces, the Boltzmann equation describing the evolution of f^* can be written as

$$\frac{\partial f^*}{\partial t} + c^* \cdot \frac{\partial f^*}{\partial \mathrm{x}} = \left[\frac{df^*}{dt}\right]_{coll} \tag{2.2}$$

where the term $\frac{\partial f^*}{\partial \mathrm{t}}$ represents the change in the number of molecule with position x^* and velocity c^*.

The term $\mathrm{c}^* \cdot \frac{\partial f^*}{\partial \mathrm{x}}$ models the convection of molecules due to velocity in the infinitesimal element $d^3\mathrm{x}^*$. Finally, the term on the right hand side represents intermolecular collisions changing the velocity distribution of the molecules.

The binary collision model for dilute gas is defined as

$$\left[\frac{df^*}{dt}\right]_{coll} = \iint \left(f_1^{*\prime} f^{*\prime} - f_1^* f^*\right) g^* \sigma^* d^2\Theta d^3 c_1^* \qquad (2.3)$$

where σ^* is the differential cross-section, Θ is the differential solid angle associated to the collision, g^* is the relative velocity of two colliding particles such that $g^* = \left|c_1^* - c^*\right| = \left|c_1^{*\prime} - c^{*\prime}\right|$ remains equal before and after collision. Note that c_1^* is the molecular velocity of the "bullet" particle that collides with a "target" particle of velocity c. c_1^* and c^* are the pre-collision velocities whereas $c_1^{*\prime}$ and $c^{*\prime}$ refer to the post-collision velocities and relate to the pre-collision velocities through angle Θ.

The first integral of equation (2.3) :

$$\iint \left(f_1^{*\prime} f^{*\prime}\right) g^* \sigma^* d^2\Theta d^3 c_1^* \qquad (2.4)$$

represents the rate of collisions that have c^* as a post-velocity. Here, the number of molecules with velocity c^* increases. The second term of Eq. (2.3) is

$$\iint \left(-f_1^* f^*\right) g^* \sigma^* d^2\Theta d^3 c_1^* \qquad (2.5)$$

and describes the rate at which molecules of velocity c^* are colliding. The negative sign indicates a reduction of the number of particles with velocity c^*. The collision integral can thus be seen as an integration of the collision rate over all possible collision pairs c_1^* and c^*, and over all solid angles Θ.

At equilibrium, the solution of the Boltzmann equation is the known Maxwell-Boltzmann distribution

$$f(c) = \left(\frac{m}{2\pi KT} \right)^{3/2} \exp\left(-\frac{mc^2}{2KT} \right) \tag{2.6}$$

where m is the mass of a particle, *K* is Boltzmann's constant, and *T* is the temperature.

The formulation presented here is limited to dilute gas as only binary collisions were considered. Nonetheless, the Boltzmann equation remains valid for all flow regimes, from Kn 0 to ∞, provided suitable collision integrals are use to model the problem. For 3D applications, this amounts to evaluating a non-linear, often discontinuous, five-dimensional integral on a seven-dimensional space (physical space, velocity space and time). Moreover, local conversation of mass, momentum and energy must be maintained throughout integration. Consequently, solving numerically the Boltzmann equation remains a major challenge. More work is required before it can be a viable option to model hypersonic flows.

2.2.2 Navier-Stokes Equations

Although the N-S equations were formulated well before the Boltzmann equation, they can be derived from the Boltzmann equation via Chapman-Enskog expansion and under the assumption of small perturbations from equilibrium. Thus limiting the validity of the N-S equations to flows near equilibrium [20].

Assuming no external forces ($F^B = 0$), the compressible, 3D N-S equations can be written in conservative form as

$$\frac{\partial Q}{\partial t} + \nabla \cdot \mathcal{F}_A(\mathbf{Q}) - \nabla \cdot \mathcal{F}_v(\mathbf{Q}) - \nabla \cdot \mathcal{F}_T(\mathbf{Q}) = 0 \tag{2.7}$$

where **Q** is the conservative state vector,

$$\mathbf{Q} = \left(\rho,\ \rho u,\ \rho v,\ \rho w,\ \rho E\right)^{T}, \tag{2.8}$$

$\mathcal{F}_{A} = \left(F_{A}^{x},\ F_{A}^{y},\ F_{A}^{z}\right)$ is the inviscid flux,

$$F_{A}^{x} = \begin{pmatrix} \rho u \\ \rho u^2 + P \\ \rho uv \\ \rho uw \\ u(E+P) \end{pmatrix}, \qquad F_{A}^{y} = \begin{pmatrix} \rho v \\ \rho uv \\ \rho v^2 + P \\ \rho vw \\ v(E+P) \end{pmatrix}, \qquad F_{A}^{z} = \begin{pmatrix} \rho w \\ \rho uw \\ \rho vw \\ \rho w^2 + P \\ w(E+P) \end{pmatrix} \tag{2.9}$$

ρ is the density, *u*, *v* and *w* are the components of velocity in the x, y and z directions, respectively, *P* is the pressure and *E* is the total energy per unit mass.

The shear stress tensor is defined as

$$\tau = \mu(\nabla \mathbf{V} + \nabla \mathbf{V}^{T}) + \eta \nabla \cdot \mathbf{V} \tag{2.10}$$

V is the velocity vector, μ is the dynamic viscosity and η is the second viscosity coefficient. The coefficients of viscosity relate to the bulk viscosity as

$$\mu_{B} = \tfrac{2}{3}\mu + \eta \tag{2.11}$$

For the present work, the bulk viscosity is assumed to be zero. The shear stress is therefore written as

$$\tau = \mu(\nabla \mathbf{V} + \nabla \mathbf{V}^{T}) - \tfrac{2}{3}\mu \nabla \cdot \mathbf{V} \tag{2.12}$$

The viscous flux $\mathcal{F}_{v} = \left(F_{v}^{x},\ F_{v}^{y},\ F_{v}^{z}\right)$, reads as

$$\mathsf{F}_v^x = \begin{pmatrix} 0 \\ \tau_{xx} \\ \tau_{xy} \\ \tau_{xz} \\ \mathbf{V}\tau_x \end{pmatrix}, \qquad \mathsf{F}_v^y = \begin{pmatrix} 0 \\ \tau_{yx} \\ \tau_{yy} \\ \tau_{yz} \\ \mathbf{V}\tau_y \end{pmatrix}, \qquad \mathsf{F}_v^z = \begin{pmatrix} 0 \\ \tau_{zx} \\ \tau_{zy} \\ \tau_{zz} \\ \mathbf{V}\tau_z \end{pmatrix}. \tag{2.13}$$

The heat flux follows Fourier's law as

$$q = -k\nabla T \tag{2.14}$$

where k is the thermal conductivity.

Finally, the thermal flux, $\mathcal{F}_{\mathsf{T}} = \left(\mathsf{F}_{\mathsf{T}}\right)$, is

$$\mathsf{F}_T = \begin{pmatrix} 0 \\ 0 \\ 0 \\ 0 \\ q \end{pmatrix}. \tag{2.15}$$

These constitute five equations with six unknowns. The final equation to obtain closure of the system is the perfect gas equation of state, given as

$$P = \rho RT \tag{2.16}$$

with R being the specific gas constant.

To extend the applicability of the N-S equation past the continuum regime (Kn > 0.01), more sophisticated numerical approaches are required.

2.3 Numerical Methods

2.3.1 Direct Simulation Monte-Carlo Methods

The direct simulation Monte Carlo method was initially developed by Bird in 1961 to model rarefied gas flows [24, 25]. It is a statistical approach based on the same physical principles behind the Boltzmann equation. Without solving the equation due to the complexity of the collision integral, it emulates the equation through an algorithm where the collision process is performed on a probabilistic basis.

The DSMC algorithm can be described in four steps. Here, the state of the system is defined by the velocities and positions of the particles. In this case, each particle is representative of a set of physical molecules. The computational domain is divided into cells where collisions between particles can only occur within particles belonging to the same cell.

1. Advection step (no collision)
    a. The position of the simulated particles is updated according to their current velocity: $\mathbf{x}^*(t^* + \Delta t^*) = \mathbf{x}^*(t^*) + \mathbf{c}^*(t^*)\Delta t^*$
    b. Particles that collided with a boundary a reflected back into the domain. Their positions and velocities are updated correspondingly.
2. Particles are sorted into cells
3. The collision process within each cell is performed
    a. Probabilistically evaluate if a collision between a pair of particle occurs. If it is evaluated positively, update the particles velocity to a post-collision value. If there is no collision, move on to a next pair of particles.

4. Evaluate macroscopic fields (velocity, temperature, heat flux, shear stress)

    a. The macroscopic quantities are computed from the appropriate weighted integral of the distribution functions:

        i. $\rho = mn = m\int f\, d^3\mathbf{c}$

        ii. $u_i = \frac{1}{n}\int c_i\, f\, d^3\mathbf{c}$

        iii. $\tau_{ij} = \frac{1}{n}\int (c_i - u_i)(c_j - u_j) f\, d^3\mathbf{c}$

        iv. $T = \frac{2}{3n}\int \left|\mathbf{c} - \mathbf{u}\right| f\, d^3\mathbf{c}$

        v. $q_i = \frac{1}{2}\int (c_i - u_i)\left|\mathbf{c} - \mathbf{u}\right| f\, d^3\mathbf{c}$

        m is the molecular mass, *n* the number density, ***u***, the fluid velocity, τ the shear stress tensor, *T* is the temperature, *q* the heat flux and the indexes i and j are the vector components.

The DSMC method is extremely efficient and accurate to model high speed rarefied flow. However, as the density increases, the number of simulated particles becomes intractable and the computational cost is prohibitively expensive. While particle-based methods, such as Direct Simulation Monte Carlo (DSMC), can be applied efficiently only to free-molecular regimes due to the limited number of particles to follow, hybrid methodologies that use N-S in regions of near-equilibrium / transitional regime, and particle-based methods in regions of rarefied flow [26-31] have been published in the literature. Such strategies, however, are subject to inaccuracies caused by the

interpolation of information at the interface between the various regions and also due to the fact that DSMC is typically subject to statistical scatter that may negatively affect the continuum-based solution. As a stratagem to delay the use of expensive particle-based methods, continuum-based CFD codes can be modified to simulate flows in the moderate non-equilibrium region (0.01 < Kn < 1) by introducing boundary conditions that account for velocity slip and temperature jump at the wall. These advanced numerical approaches are necessary to accurately simulate near-wall aerothermodynamics phenomena.

2.3.2 Computational Fluid Dynamics

CFD techniques are used to solve the N-S equations numerically. While there are various methods to solve these equations, such as Finite Volume and Finite Difference schemes, the focus will be on the Finite Element Method.

From section 2.2.2, the N-S equations read as

$$\frac{\partial Q}{\partial t} + \nabla \cdot \left(\mathcal{F}_A - \mathcal{F}_v - \mathcal{F}_T \right) = 0 \tag{2.17}$$

Consider a tessellation over a domain Ω resulting in a set of non-overlapping elements Ω_i. Introducing the Galerkin variational principle, a set of linear test functions W_i belonging to $V \subset H^1(\Omega)$ and integrating over the domain Ω as follows

$$\int_{\Omega} W_i \frac{\partial Q}{\partial t} + \int_{\Omega} \nabla W_i \cdot \left(\mathcal{F}_A - \mathcal{F}_v - \mathcal{F}_T \right) = 0 \tag{2.18}$$

After integration by parts, the weak-Galerkin formulation for the N-S equations is obtained

$$\int_{\Omega} W_i \frac{\partial Q}{\partial t} - \int_{\Omega} \nabla W_i \cdot \left(\mathcal{F}_A - \mathcal{F}_v - \mathcal{F}_T \right) + \int_{\partial\Omega} W_i \mathbf{n} \cdot \left(\mathcal{F}_A - \mathcal{F}_v - \mathcal{F}_T \right) = 0 \quad (2.19)$$

Introducing Lagrangian shape functions, N_j and nodal vectors **Q** and $\mathcal{F}_A$

$$\begin{aligned} Q(t,\boldsymbol{x}) &= \sum_{j=1}^{N_G} N_j(\mathbf{x}) Q_j(t) & \mathcal{F}_A(t,\mathbf{x}) &= \sum_{j=1}^{N_G} N_j(\mathbf{x}) \mathbf{F}_j^A(t) \\ \mathcal{F}_v(t,\mathbf{x}) &= \sum_{j=1}^{N_G} N_j(\mathbf{x}) \mathbf{F}_j^V(t) & \mathcal{F}_T(t,\mathbf{x}) &= \sum_{j=1}^{N_G} N_j(\mathbf{x}) \mathbf{F}_j^T(t) \end{aligned} \quad (2.20)$$

where N_G is the number of nodes in the mesh, N_j are the Lagrange shape functions of the *j*-th vertex. $\mathbf{Q}_j$ and $\mathbf{F}_j^A$ are the values of *Q* and $\mathcal{F}_A$ at the *j*-th node of the grid.

The Finite Element representation of the N-S equations is obtained by substituting Eq. 2.19 into Eq. 2.20.

$$\sum_{j=1}^{N_G} \int_{\Omega} W_i N_j \frac{dQ_j}{dt} - \sum_{j=1}^{N_G} \int_{\Omega} N_j \nabla W_i \cdot \mathbf{F}_j + \int_{\Omega} \nabla W_i \cdot (\mathbf{F}^V + \mathbf{F}^T) + \int_{\partial\Omega} W_i \mathbf{n} \cdot (\mathbf{F}^A - \mathbf{F}^V - \mathbf{F}^T) = 0 \quad (2.21)$$

In the Galerkin formulation, the weight functions are selected equal to the shape functions, $W_j(\mathbf{x}) = N_j(\mathbf{x})$. This equation can be further discretized be substituting the integral over the domain Ω by a summation over the elements of the triangulation Ω_e,

$$\begin{aligned} \sum_{e \in E_i} \sum_{j \in K_e} \int_{\forall_e} W_i N_j \frac{dQ_j}{dt} d\forall - \sum_{e \in E_i} \sum_{j \in K_e} \int_{\forall_e} N_j \nabla W_i \cdot \mathbf{F}_j \, d\forall + \sum_{e \in E_i} \int_{\Omega} \nabla W_i \cdot (\mathbf{F}^V + \mathbf{F}^T) d\forall \\ + \sum_{e \in F_i} \int_{A} W_i \mathbf{n} \cdot (\mathbf{F}^A - \mathbf{F}^V - \mathbf{F}^T) \, dA = 0 \end{aligned} \quad (2.22)$$

where E_i is the set of elements connected to the *i*-th node, F_i is the set of boundary faces connected to the *i*-th node, and K_e is the set of nodes of the *e*-th element.

In the CFD solver used in this Thesis, HALO3D (High Altitude-Low Orbit), the domain integral is performed in an edge-based fashion. The formulation will not be derived. For more details, the reader is directed to this text [32].

Chapter 3 Non-Equilibrium Boundary Conditions

3.1 Gas Surface Interactions

The aerothermodynamics of a vehicle are dictated by the momentum and energy transfer of the flow of gas interacting with the surface of the vehicle [33]. Consequently, the physical / numerical modeling of these interactions directly affects the boundary conditions to be used in the numerical model [34].

3.1.1 Kinetic Theory

In the kinetic theory, the impinging particle on the surface is reflected either elastically (specular) or diffusely. In perfectly specular reflection, the particles are reflected with a normal velocity in the opposite direction while the tangential velocity remains the same. The wall shear stress and heat fluxes are then zero. Conversely, for purely diffusive reflection, the molecule colliding with the wall is re-emitted at a random angle and a velocity corresponding the Maxwell velocity distribution at equilibrium. A portion of the momentum and energy of the incident molecule is lost to the surface and therefore shear stress and heat flux at the wall are non-zero [33]. In practice for real surfaces, some molecules will reflect diffusely while others will reflect elastically. The accommodation coefficient is defined as the ratio of incident particles reflected diffusely and depends heavily on the surface and gas types. In general, the accommodation coefficient is given by

$$\sigma = \frac{\Phi_i^f - \Phi_r^f}{\Phi_i^f - \Phi_w^f} \tag{3.1}$$

where Φ_i^f and Φ_r^f represent the incident and reflected flux of either the tangential momentum or the energy. Φ_w^f represents the reflected flux accommodating fully the solid surface [33]. It will be described further in section 3.3.

3.1.2 Langmuir Adsorption Approach

In this model, the impinging molecules (adsorbate) bind to distinct sites onto the solid surface (adsorbent) creating a film of molecules [35]. This physical approach based on surface chemistry theory is called adsorption. According to Langmuir's model, an impinging particle either sticks permanently to a surface via physisorption or chemisorption or sticks temporary and leave the surface once thermal equilibrium is reached. Expressing this process as a reaction gives

$$A_g + S \leftrightarrow A_{ad} \tag{3.2}$$

where A_g is a gas molecule reacting with an empty site S to form the adsorbed complex A_{ad}. The fraction of molecule sticking to the surface can be obtained by deriving an equilibrium expression for the adsorption of a gas. Based on this model, Langmuir boundary conditions can be derived (section 3.2).

3.2 Velocity Slip and Temperature Jump

Several formulations of the slip and jump conditions based on the kinetic theory of gases have been proposed in the literature, following the seminal work of Maxwell [30, 36-44]. Most of the available slip models are extensions of the Maxwell formulation and neglect the gradient of velocity normal to the wall; consequently they are not easily applicable to geometries with strong curvature or for rotational motion [36-38]. A more

general formulation of the Maxwell velocity slip that can be applied to complex geometries is used in this work by considering the full form of the tangential shear stress, which naturally contains a term for the variation of the velocity normal to the body in the tangential direction. A brief review of slip models will be given as well for the purpose of self-containment.

Maxwell Velocity Slip

In the original formulation of Maxwell [39], the velocity tangential to the wall is expressed in terms of the tangential components of shear stress and heat flux, $\boldsymbol{\tau}_{slip}$ and $\boldsymbol{q}_{slip}$. The wall slip velocity is thus

$$\mathbf{V}_{slip} = -\frac{\lambda}{\mu}\frac{2-\sigma_V}{\sigma_V}\boldsymbol{\tau}_{slip} - \frac{3}{4}\frac{(\gamma-1)\mathrm{Pr}}{\gamma P}q_{slip} \tag{3.3}$$

where σ_V is the tangential momentum accommodation coefficient, μ is the dynamic viscosity at the wall, λ is the molecular mean-free-path at the wall, Pr is the Prandtl number, γ is the specific heat ratio and P is the gas pressure. The momentum accommodation coefficient σ_V represents the fraction of momentum lost by the gas molecules that are reflected diffusely when colliding with the wall. Experiments indicate that the momentum accommodation coefficient ranges between 0.2 and 0.8 [45, 46]. The mean-free-path is defined as:

$$\lambda = \frac{\mu}{\rho}\sqrt{\frac{\pi}{2RT}} \tag{3.4}$$

where ρ is the density, T is the temperature and R the gas constant. Equation (3.3) can be expressed in terms of wall shear stress, $\boldsymbol{\tau}_w$, and temperature gradient, ∇T_w, as:

$$\mathbf{V}_{slip} = -\frac{\lambda}{\mu}\frac{2-\sigma_V}{\sigma_V}(\mathbf{n}\cdot\tau_w)(\mathbf{I}-\mathbf{nn}) - \frac{3}{4}\frac{(\gamma-1)\mathrm{Pr}}{\gamma P}(k\nabla T_w - (k\nabla T_w\cdot\mathbf{n})\mathbf{n}) \qquad (3.5)$$

n being the unit-vector normal to the wall and *k* being the thermal conductivity. In Eq. (3.5) the vector-tensor dot product is defined as

$$(\mathbf{n}\cdot\boldsymbol{\tau})^{\alpha} = \sum_{\beta=1}^{3} n^{\beta}\tau^{\beta\alpha} \qquad \text{and} \qquad (\boldsymbol{\tau}\mathbf{n})^{\alpha} = \sum_{\beta=1}^{3} \tau^{\alpha\beta}n^{\beta} \qquad (3.6)$$

The vector-vector outer product is also introduced here as ***c=ab,*** such that $c^{\alpha\beta} = a^{\alpha}b^{\beta}$. The Cartesian components of a vector/tensor being indicated with a superscript Greek letter, to distinguish them from the vertex index, i.e. a subscript Latin letter.

Smoluchowski Temperature Jump

The Smoluchowski's formulation for the temperature jump [47] is

$$T_{slip} - T_{wall} = \left(\frac{2-\sigma_T}{\sigma_T}\right)\frac{2\gamma}{(\gamma+1)\mathrm{Pr}}\lambda\nabla T\cdot\mathbf{n} \qquad (3.7)$$

where σ_T is the temperature accommodation coefficient and T_{wall} is the temperature at the wall. The thermal accommodation coefficient σ_T is defined as the fraction of energy exchanged between the gas molecules and the surface. Studies show that it generally ranges between 0.3 - 0.9 [45, 46, 48]. A coefficient of unity will be used throughout this study to match the fully diffuse wall used in the simulations of the reference data [15, 49].

Wall-Function Approach

The N-S equations are based under the assumption that the shear stress varies linearly with the velocity gradients. In the Knudsen layer, a local region of non-

equilibrium extending a few mean free paths away from the surface, the N-S equations cannot model the non-linear stress / strain-rate behavior of the flow [50]. Following the original work of Cercignani, Lockerby et al. [41] proposed a curved-fitted approximation correction to the viscosity in function of the normal distance to the surface given by

$$\psi\left(\frac{y}{\lambda}\right) \approx 1 + \frac{7}{10}\left(1 + \frac{y}{\lambda}\right)^{-3} \tag{3.8}$$

where y is the normal distance to the wall. The effective viscosity is computed as

$$\mu = \frac{\mu}{\psi} \tag{3.9}$$

The wall-function given in (3.8) should by used in conjunction with Maxwell velocity slip (Eq. 3.3) allowing accurately simulating the velocity profile and capturing the non-linear behavior. However this model is limited to low-Knudsen / low-Mach numbers flows over planar surface and does not consider accommodation coefficients.

Langmuir Slip Model

Alternative boundary conditions developed by Myong and colleagues [42, 51, 52] for rarefied gas microflows and based on Langmuir adsorption theorem can be expressed as

$$\begin{aligned} \mathbf{V}_{slip} &= \alpha_M \mathbf{V}_{wall} + (1-\alpha_M)\mathbf{V}_{loc} \\ T_{slip} &= \alpha_M T_{wall} + (1-\alpha_M) T_{loc} \end{aligned} \tag{3.10}$$

where the *loc* subscript denotes a reference value of the gas taken one or two mean free-paths away from the surface, $\mathbf{V}_{wall}$ and T_{wall} are the velocity at the wall and the

temperature at the wall respectively and α_M is the fraction of the surface covered by adsorbed atoms at thermal equilibrium calculated as [51]

$$\alpha_M = \frac{\beta p}{1+\beta p} \tag{3.11}$$

for monoatomic gas and

$$\alpha_M = \frac{\sqrt{\beta p}}{1+\sqrt{\beta p}} \tag{3.12}$$

for diatomic gas. The parameter β is a function of the wall temperature T_{wall} and the heat of adsorption D_e and can be computed as follows

$$\beta = \frac{A\lambda}{R_u T_{wall}} \exp\left(\frac{D_e}{R_u T_{wall}}\right) \tag{3.13}$$

where R_u is the universal gas constant and A is the mean area of a site; it is measured or approximated by $A = N_A \pi d^2/4$, d being the diameter of the molecule and N_A the Avogadro Number ($N_A = 6.022140857 \times 10^{23}$). One limitation of these slip conditions lies on the choice of the reference values (denoted by the subscript *loc* in eq. (3.10)) that can be evaluated either one or two mean free-paths away from the surface or in the freestream region [42]. As Le et al. concluded that the Langmuir model did not provided particularly good results for hypersonic aerodynamics, these slips will not be investigated [42].

3.3 Slip Coefficient

The tangential momentum accommodation coefficient (TMAC) σ_V represents the fraction of the gas molecules that are reflected diffusely when colliding with the wall. A TMAC of 0 represents an infinitely smooth surface, while a TMAC equals to 1 represents a rough wall with only diffuse interactions (fully diffuse wall). Experiments indicate that the TMAC varies with the molecular weight of the gas, the surface material, the temperature and roughness of the surface. More recently, Sharipov and Seleznev [53] developed an expression for the velocity slip derived from kinetic analysis on curved surfaces [54]. By neglecting the thermal creep, the Maxwell velocity slip, Eq. (3.3), is re-written as

$$\mathbf{V}_{slip} = -\frac{\lambda}{\mu} A_\sigma \boldsymbol{\tau}_{slip} \tag{3.14}$$

where A_σ is a coefficient defined as

$$A_\sigma = \frac{2}{\sqrt{\pi}} \sigma_P \tag{3.15}$$

and, for planar flow, the slip coefficient, σ_P, can be written as

$$\sigma_P(\sigma_V) = \left(\frac{2-\sigma_V}{\sigma_V} \right) \left[\sigma_P(1) - 0.1211(1-\sigma_V) \right] \tag{3.16}$$

Albertoni et al. [55] derived a value for $\sigma_P(1)$ of 1.016191 from the Bhatnagar–Gross–Krook (BGK) model of the Boltzmann equation, which is commonly referred to as the most accurate value for $\sigma_P(1)$ in fully diffuse conditions. Using these values in (3.15), A_σ equates to 1.14665 in this case. It will not be used in this work, instead a simple

TMAC of one will be used throughout this study to remain consistent with the available data [15, 49].

3.4 Numerical Implementation of the Boundary Conditions

Given the formulations described above, we first present the Dirichlet formulation and procedure to impose the non-equilibrium boundary conditions. Then, the Robin formulation of the temperature jump and velocity slip is summarized.

3.4.1 Dirichlet Boundary Conditions

Equation (3.5) and equation (3.7) can be enforced as Dirichlet conditions with the following procedure, illustrated in Figure 3.1.

a. Assembly of the residuals and the Jacobian matrix of the N-S equations.
b. Imposition of a Dirichlet condition for the temperature and velocity based on their current value using relaxation.
c. Solution of the Newton step and update of the conservative variables, with $\mathbf{\Delta}T = 0$ and $\mathbf{\Delta V} = 0$.
d. Computation of the normal shear stress and heat flux via the Consistent Galerkin approach (see section 4.2).
e. Update of the velocity and temperature field at the wall using equations (3.5) and (3.7), respectively.

The procedure is repeated until convergence.

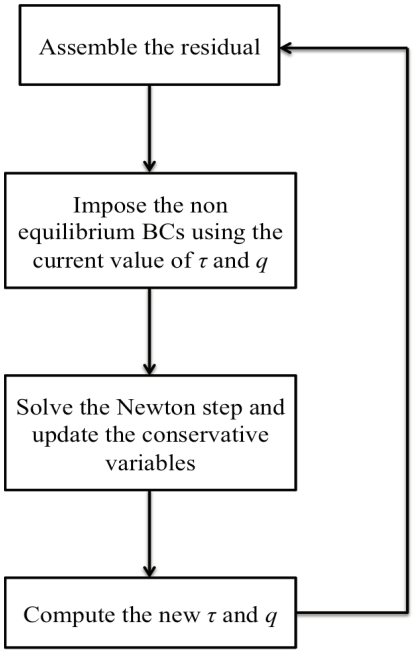

Figure 3.1. Algorithm for the imposition of the velocity slip and temperature jump using the Consistent Galerkin approach.

3.4.2 Robin Boundary Conditions

In the absence of thermal creep, the velocity slip can be reformulated as

$$\mathbf{n}\cdot\tau = -\frac{\sigma_V}{2-\sigma_V}\frac{\mu}{\lambda}\mathbf{V}_{slip} + (\mathbf{n}\cdot\tau)\cdot\mathbf{nn} \tag{3.17}$$

This formulation gives a condition for the shear stress. The vectors appearing above are rewritten component by component making use of Einstein's notation as

$$(n\cdot\tau)^{\alpha} = n^{\beta}\tau^{\beta\alpha}, \qquad \left((n\cdot\hat{\tau})\cdot(nn)\right)^{\alpha} = n^{\gamma}\tau^{\gamma\beta}n^{\beta}n^{\alpha} \qquad \text{and} \qquad \left((V\cdot n)n\right)^{\alpha} = V^{\beta}n^{\beta}n^{\alpha}$$

$$(\mathbf{n}\cdot\tau) = (\mathbf{nn}:\nabla\mathbf{V})\mathbf{n} - \frac{\sigma_V}{2-\sigma_V}\frac{\mu}{\lambda}\mathbf{V}_t \tag{3.18}$$

In the same manner, considering the temperature jump

$$T_i = T_{wall} - \frac{2-\sigma_T}{\sigma_T}\frac{2\gamma}{\gamma+1}\frac{\lambda}{k}\frac{\mathbf{q}\cdot\mathbf{n}}{\mathrm{Pr}} \qquad \text{with} \qquad \mathbf{q}\cdot\mathbf{n} = -k\nabla T \tag{3.19}$$

The heat flux is thus

$$\mathbf{n}\cdot\mathbf{q} = -\mathrm{Pr}\frac{k}{\lambda}\frac{\gamma+1}{2\gamma}\frac{\sigma_T}{2-\sigma_T}\left(T_i - T_{wall}\right) \tag{3.20}$$

The velocity slip and temperature jump are now reformulated as Robin boundary conditions. The FE methodology has a mathematical infrastructure that provides more rigorous and accurate ways to define these types of boundary conditions.

At steady-state, the weak-Galerkin form of the momentum equations are

$$-\int_\Omega \nabla W_i \cdot\left(\mathbf{F}-\tau\right)+\int_{\partial\Omega} W_i\,\mathbf{n}\cdot\mathbf{F}-\int_{\partial\Omega} W_i\,\mathbf{n}\cdot\tau = 0 \tag{3.21}$$

The energy equation reads as

$$-\int_\Omega \nabla W_i \cdot\left(\rho h\mathbf{V}-\mathbf{V}\cdot\tau-k\nabla T\right)+\int_{\partial\Omega} W_i\,\mathbf{n}\cdot\left(\rho h\mathbf{V}\right)-\int_{\partial\Omega} W_i\,\mathbf{n}\cdot\left(\mathbf{V}\cdot\tau-k\nabla T\right) = 0 \tag{3.22}$$

Applying the Robin boundary conditions, the equations become

$$-\int_\Omega \nabla W_i \cdot\left(\mathbf{F}-\tau\right)+\int_{\partial\Omega} W_i\,\mathbf{n}\cdot\mathbf{F}-\int_{\partial\Omega} W_i\left[(\mathbf{nn}:\nabla\mathbf{V})\mathbf{n}-\frac{\sigma_V}{2-\sigma_V}\frac{\mu}{\lambda}\mathbf{V}_t\right] = 0 \tag{3.23}$$

and,

$$\begin{aligned}-\int_\Omega \nabla W_i \cdot\left(\rho h\mathbf{V}-\mathbf{V}\cdot\tau-k\nabla T\right)+\int_{\partial\Omega} W_i\,\mathbf{n}\cdot\left(\rho h\mathbf{V}\right)-\int_{\partial\Omega} W_i\,\mathbf{V}\cdot\left[(\mathbf{nn}:\nabla\mathbf{V})\mathbf{n}-\frac{\sigma_V}{2-\sigma_V}\frac{\mu}{\lambda}\mathbf{V}_t\right]\\ +\int_{\partial\Omega} W_i\left(\mathrm{Pr}\frac{k}{\lambda}\frac{\gamma+1}{2\gamma}\frac{\sigma_T}{2-\sigma_T}\left(T_i-T_{wall}\right)\right) = 0\end{aligned} \tag{3.24}$$

Provided that the contour domain is the surface of a body. Otherwise, the regular equations will prevail.

Under this formulation, the non-equilibrium boundary conditions are implemented in a more natural manner. For the present work, the Dirichlet implementation is

followed to take advantage of the higher accuracy achieved by the Consistent Galerkin approach.

Chapter 4 Consistent Galerkin Methodology

The computational cost, in terms of time and computational resources, to obtain adequate accuracy for engineering purpose often constitutes a major constraint on the application of CFD to aerothermodynamics design. One solution is to use higher accuracy methods to decrease the computational footprint necessary to achieve an acceptable error level by alleviating the grid spacing requirements. The following section conveys the fundamental concepts of the Consistent Galerkin methodology for the computation of shear stress and heat flux.

4.1 Direct Approach

The velocity slip and temperature jump equations require the evaluation of temperature gradients and shear stresses at the walls. While there are multiple ways to compute such quantities [19, 49, 56-58] with the finite volume and finite difference discretizations, extended stencils comprising more than two points are required to get at least second order accuracy. This can be done on structured meshes with one-sided discretization stencils, provided that strict orthogonality is maintained near the wall, but the approach is not generalizable to unstructured meshes. In the FE framework the most immediate way to compute the shear stress and heat flux would be by a direct differentiation of the shape functions at the wall. For a Newtonian fluid, the tensor of the normal viscous stresses is written as

$$\tau_{\mathbf{n}} = \mathbf{n}\cdot\tau = \mu\left(\mathbf{n}\cdot\nabla\mathbf{V} + (\nabla\mathbf{V})\mathbf{n}\right) - \tfrac{2}{3}\mu\mathbf{n}\nabla\cdot\mathbf{V} \qquad (4.1)$$

Lagrangian shape functions, N_j, are used to approximate the velocity throughout each element as a linear combination of the values at the vertices, i.e.

$$\mathbf{V}(t,\mathbf{x}) = \sum_{j=1}^{N_G} N_j(\mathbf{x}) V_j(t) \tag{4.2}$$

where N_G is the number of nodes in the mesh, N_j are the Lagrange shape functions of the j-th vertex and $\mathbf{V}_j$ is the value of velocity vector at the j-th node. Substituting the polynomial expansion of the velocity into equation 4.1, one obtains

$$\tau_{\mathbf{n}} = \sum_{j=1}^{N} \mathbf{V}_j \cdot \left[\mu(\mathbf{n}\cdot\nabla N_j + \mathbf{n}\nabla N_j) - \tfrac{2}{3}\mu(\nabla N_j \mathbf{n}) \right] \tag{4.3}$$

or, by components

$$(\tau_{\mathbf{n}})^{\alpha} = \sum_{j=1}^{N} \mathrm{V}_j^{\alpha} \cdot \left[\mu(\mathrm{n}^{\gamma} \frac{\partial N_j}{\partial x^{\gamma}} + \mathrm{n}^{\alpha} \frac{\partial N_j}{\partial x^{\beta}}) - \frac{2}{3}\mu(\mathrm{n}^{\beta} \frac{\partial N_j}{\partial x^{\alpha}}) \right] \tag{4.4}$$

Following the same finite element methodology, the gradient of temperature can be approximated as

$$\nabla T_{\mathbf{n}} = \sum_{j=1}^{N} T_j \left[\mathbf{n}\cdot\nabla N_j \right] \tag{4.5}$$

The formulation just presented is only first-order accurate in space for linear finite elements. Higher accuracy can be achieved without widening the computational stencil but necessitates higher order elements where the degrees of freedom must be kept at a moderate level.

4.2 Consistent Galerkin Methodology

In order to avoid resorting to higher order elements, second order accuracy can be achieved by considering, for each component of $\boldsymbol{\tau}_n$, the corresponding momentum equation in its discretized weak-Galerkin form. Consider the conservation of momentum in the *x*-direction for a compressible fluid

$$\frac{\partial \rho u}{\partial t} + \nabla \cdot (\mathbf{F} - \tau_x) = 0 \tag{4.6}$$

where **F** represent the inviscid flux vector and $\boldsymbol{\tau}_x$ is the stress vector in the *x*-direction. Introducing a set of linear weight functions W_i and integrating by parts, Eq. 4.6 becomes

$$\int_\Omega W_i \frac{\partial \rho u}{\partial t} - \int_\Omega \nabla W_i \cdot (\mathbf{F} - \tau_x) + \int_{\partial\Omega} W_i \mathbf{n} \cdot (\mathbf{F} - \tau_x) = 0 \tag{4.7}$$

At steady state, the x-component of the stresses normal to the surface can be written as

$$\int_{\partial\Omega} W_i \mathbf{n} \cdot \tau_x = -\int_\Omega \nabla W_i \cdot (\mathbf{F} - \tau_x) + \int_{\partial\Omega} W_i \mathbf{n} \cdot \mathbf{F} \tag{4.8}$$

Only the first layer of elements near walls needs to be considered and the right-hand-side is constructed during the assembly of the momentum equations. The solution of equation 4.8 yields the nodal values of the normal shear stress tensor projected along the x-coordinate. The same approach is applied to the calculation of the wall temperature gradient. The weak-Galerkin form of the energy equation is

$$\int_\Omega W_i \frac{\partial \rho e}{\partial t} - \int_\Omega \nabla W_i \cdot (\rho h \mathbf{V} - \mathbf{V} \cdot \tau - k \nabla T) + \int_{\partial\Omega} W_i \mathbf{n} \cdot (\rho h \mathbf{V} - \mathbf{V} \cdot \tau - k \nabla T) = 0 \tag{4.9}$$

where *h* is the total enthalpy per unit mass and *e* is the total energy per unit mass. At steady state, the normal heat flux at the wall is thus

$$\int_{\partial\Omega} W_i \mathbf{n}\cdot k\nabla T = -\int_{\Omega} \nabla W_i \cdot (\rho h\mathbf{V} - \mathbf{V}\cdot\tau - k\nabla T) + \int_{\partial\Omega} W_i \mathbf{n}\cdot(\rho h\mathbf{V} - \mathbf{V}\cdot\tau) \qquad (4.10)$$

The same methodology outlined for the normal shear stresses can be used to obtain $\mathbf{n}\cdot k\ \nabla T$ at surface nodes.

4.3 Numerical Implementation of the Consistent Galerkin Approach

In order to avoid resorting to the edge-based formulation, equation 4.8 is represented as

$$\sum_{e\in F_i}\int_A W_i \mathbf{n}\cdot(\tau_x)\,dA = -\left\{\mathbf{R}^{\text{internal}} + \mathbf{R}^{\text{boundary, inviscid}}\right\} \qquad (4.11)$$

where F_i is the set of boundary faces connected to the i-th node and $\mathbf{R} = \mathbf{R}^{\text{internal}} + \mathbf{R}^{\text{boundary, inviscid}}$ is the spatial residual vector, combining the residuals from the internal elements and the boundary elements.

Discretizing further the left-hand-side by interpolating the shear stress inside the elements

$$\sum_{e\in E_i}\sum_{j\in K_e}\left(\int_{A_e} W_i N_j \mathbf{n}\,dA\right)\cdot\tau_{x_j} = -\left\{\mathbf{R}^{internal} + \mathbf{R}^{boundary,\,inviscid}\right\} \qquad (4.12)$$

where E_i is the set of elements connected to the i-th node and K_e is the set of nodes of the e-th element. Using the unit sum property of the finite-element shape functions the equation above becomes

$$\sum_{e\in E_i}\sum_{j\in K_e}\left(\int_{A_e} W_i N_j \mathbf{n}\,dA\right)\cdot\left(\tau_{x_j} - \tau_{x_i}\right) + \sum_{e\in E_i}\left(\int_{A_e} W_i \mathbf{n}\,dA\right)\cdot\tau_{x_i} = -\left\{\mathbf{R}^{internal} + \mathbf{R}^{boundary,\,inviscid}\right\} \qquad (4.13)$$

To simplify the notation,

$$\xi_i = \int_A W_i \mathbf{n}\, dA \qquad \text{and} \qquad \chi_{ij} = \sum_{e \in E_i} \int_{A_e} W_i N_j \mathbf{n}\, dA \tag{4.14}$$

The equation can then be re-written as

$$\sum_{j \in K_i} \chi_{ij} \cdot \left(\tau_{x_j} - \tau_{x_i} \right) + \xi_i \cdot \tau_{x_i} = -\left\{ \mathbf{R}^{internal} + \mathbf{R}^{boundary,inviscid} \right\} \tag{4.15}$$

Assuming that the shear stress is normal to the surface,

$$\left\| \xi_i \right\| \tau_{x_i} + \sum_{j \in K_i} \left\| \chi_{ij} \right\| (\tau_{x_j} - \tau_{x_i}) = -\left\{ \mathbf{R}^{internal} + \mathbf{R}^{boundary,inviscid} \right\} \tag{4.16}$$

Replacing the left-hand-side of the equation above by its lumped counterpart, the x-component of the shear stress is computed as

$$\tau_{x_i} = \frac{R_i^{internal} + R_i^{boundary,inviscid}}{\left\| \xi_i \right\|} \tag{4.17}$$

The computational cost for this procedure is remarkably small: indeed the residual of the wall nodes is stored during the assembly phase of the linear system for the flow equations and the mass matrix that is naturally yielded by the Galerkin method is replaced by its lumped counterpart. The order of accuracy of the heat flux and shear stress so calculated is nominally second-order and is generally superior to direct differentiation of the solution.

4.4 Order of Accuracy

In this section, the order of accuracy of the proposed methodology and the direct approach is evaluated for the heat flux and the shear stress. The analysis is performed

through a sequential grid refinement using nested uniformly-refined meshes (Figure 4.1), for the flow of argon over a cylinder at Kn = 0.01; a simulation described in chapter 5.

In the FE context, the L_2 norm for the heat flux is computed as:

$$L_2(\partial\Omega) = \left[\frac{\int_{\partial\Omega} \left(q - q_{exact}\right)^2 dA}{\int_{\partial\Omega} dA} \right]^{1/2} = \left[\frac{\sum_{i=1}^{N} \left(q - q_{exact}\right)^2 \left|A_i\right|}{\sum_{i=1}^{N} \left|A_i\right|} \right]^{1/2} \qquad (4.18)$$

where the norm is integrated over the area since the heat flux is defined strictly on the surface. A similar formulation is used to compute the L_2 norm for the shear stress. Below is the L_2 norm for the x-component of shear stress.

$$L_2(\partial\Omega) = \left[\frac{\int_{\partial\Omega} \left(\tau_x - \tau_{x_{exact}}\right)^2 dA}{\int_{\partial\Omega} dA} \right]^{1/2} = \left[\frac{\sum_{i=1}^{N} \left(\tau_x - \tau_{x_{exact}}\right)^2 \left|A_i\right|}{\sum_{i=1}^{N} \left|A_i\right|} \right]^{1/} \qquad (4.19)$$

The error is computed using the reference solution obtained from the mesh with the highest resolution. Table 4.1 presents the computational details of the four successively refined grids.

Grid	Grid spacing: h	Elements	Nodes	Surface nodes
1	8	4,000	8,160	80
2	4	16,000	32,320	160
3	2	64,000	128,640	320
4	1	256,000	513,280	640

Table 4.1. Details of the meshes used for the grid refinement analysis.

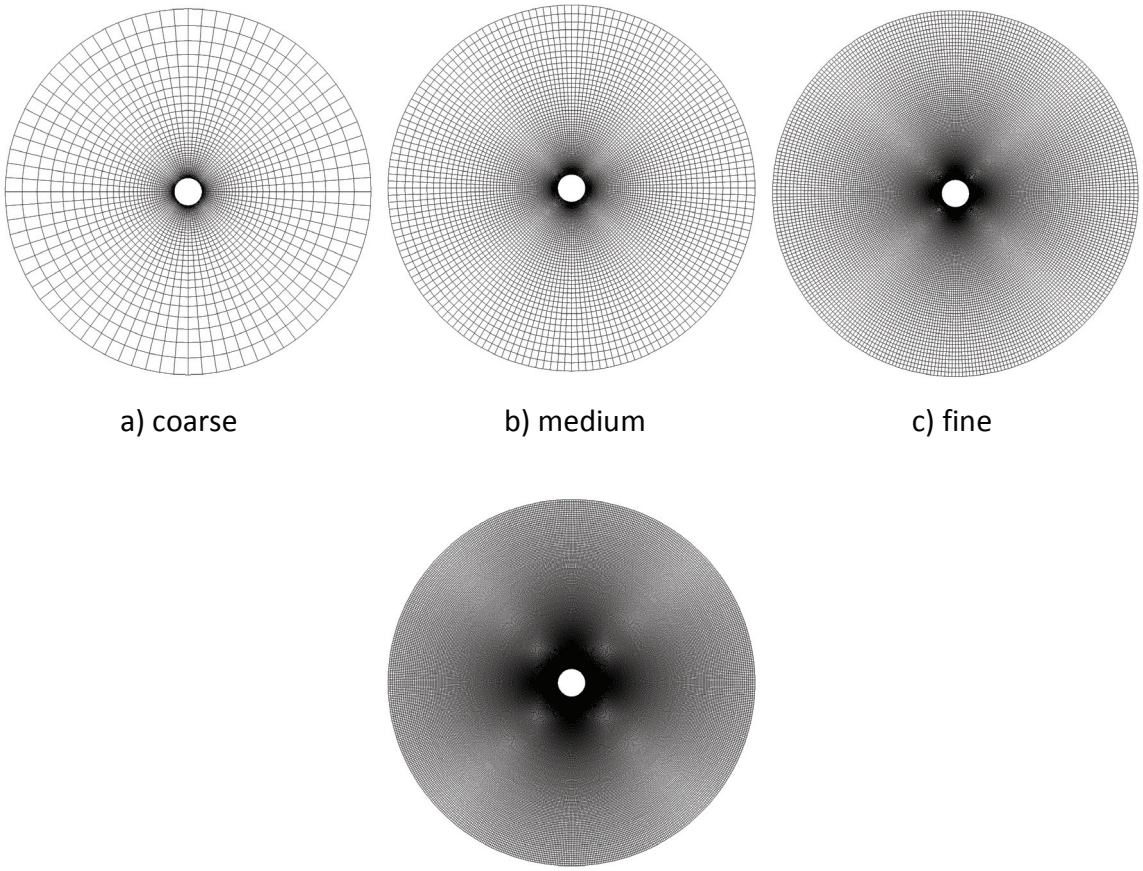

a) coarse b) medium c) fine

d) finest

Figure 4.1.Four grids across three uniform mesh refinements

Figure 4.2 shows the results of the convergence study for the heat flux. Using nonlinear least-squares algorithm for the fitting model, an order of accuracy of 0.95 is achieved for the direct approach, and an order of accuracy of 1.77 for the Consistent Galerkin methodology. The expected order of accuracy is achieved for both schemes, with the Consistent Galerkin methodology showing improved performance over the direct approach. Figure 4.3 compares the surface heating coefficient obtained by both approaches on the four different meshes. The advantage of using a higher order scheme is readily apparent: The solution of the Consistent Galerkin methodology on the coarsest

grid is more accurate than the solution of the direct approach on a mesh 8 times denser. Figure 4.4 and Figure 4.5 present the order of accuracy for the x-component and y-component of shear stress respectively while Figure 4.6 shows the resulting surface friction coefficient for both methodologies. The slope obtained from the linear fit of the results yields an order of accuracy of 1.62 for the x-component and 1.63 for the y-component of shear stress for the Consistent Galerkin methodology, demonstrating the robustness of the methodology. Indeed, the accuracy of the methodology is not overly contaminated by the presence of the shock.

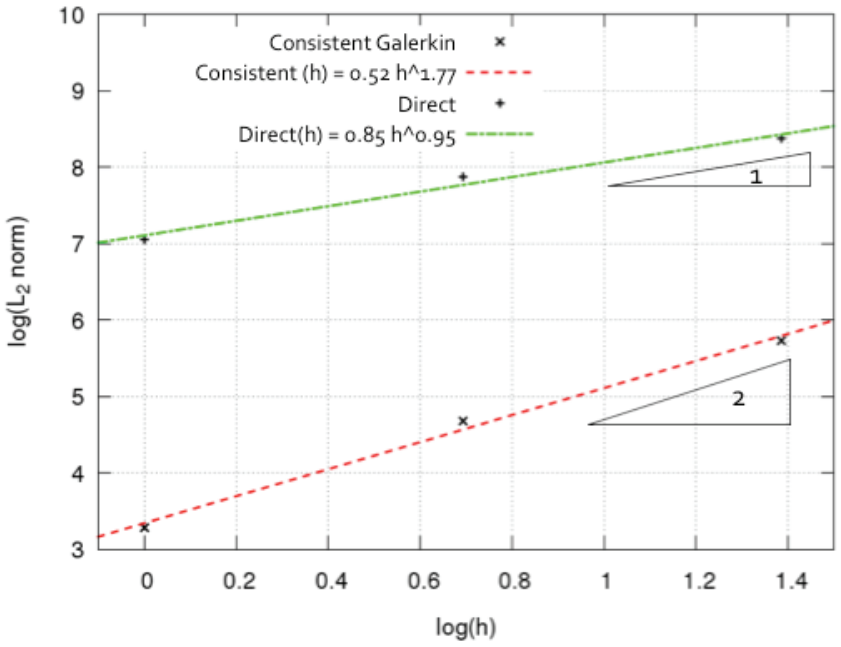

Figure 4.2. Flow of argon over a cylinder at Kn = 0.01: order of accuracy of the heat flux.

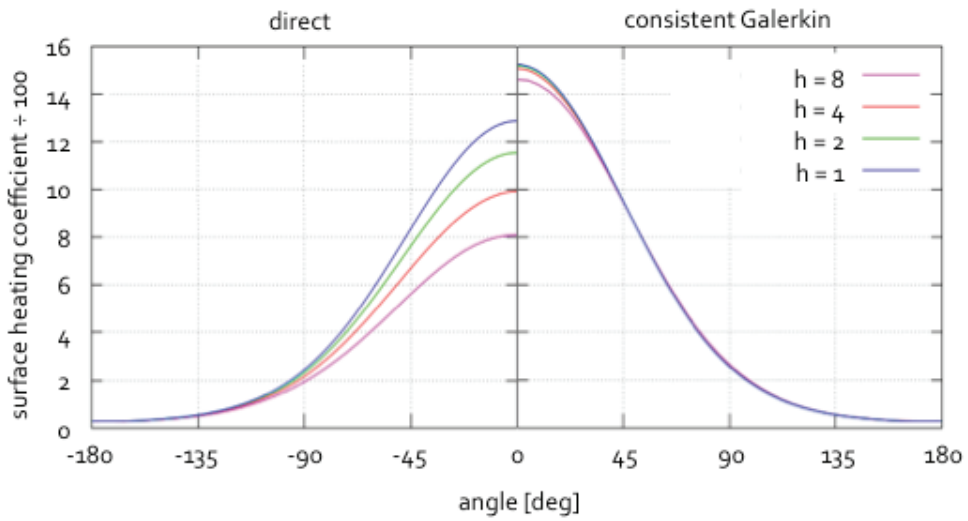

Figure 4.3. Direct approach for the surface heating coefficient (left) and Consistent Galerkin for the surface heating coefficient (right) on uniformly-refined meshes.

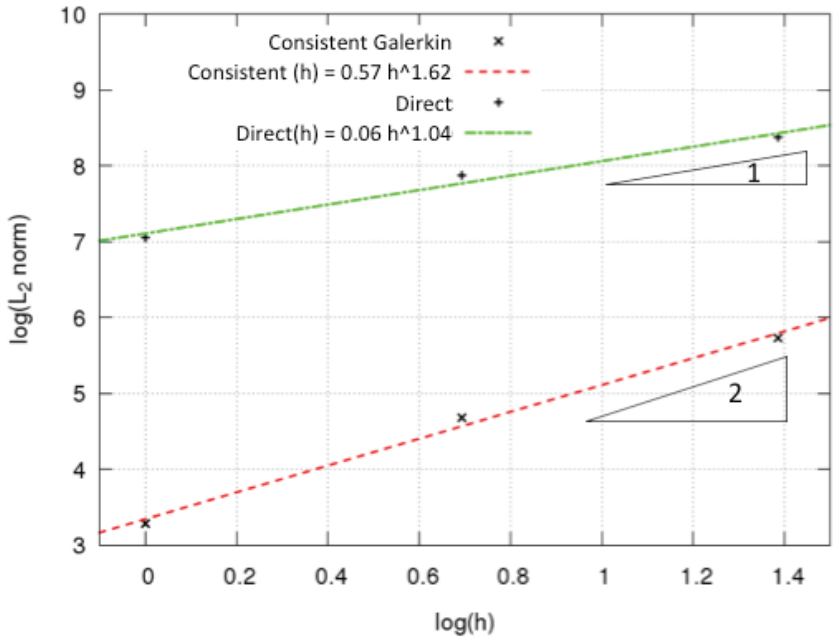

Figure 4.4. Flow of argon over a cylinder at Kn = 0.01: order of accuracy of the x-component of shear stress.

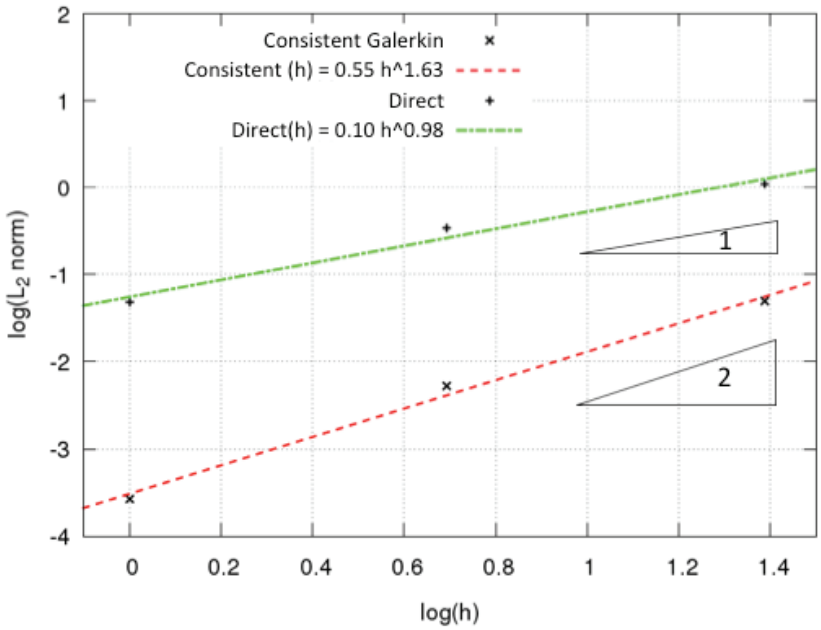

Figure 4.5. Flow of argon over a cylinder at Kn = 0.01: order of accuracy of the y-component of shear stress.

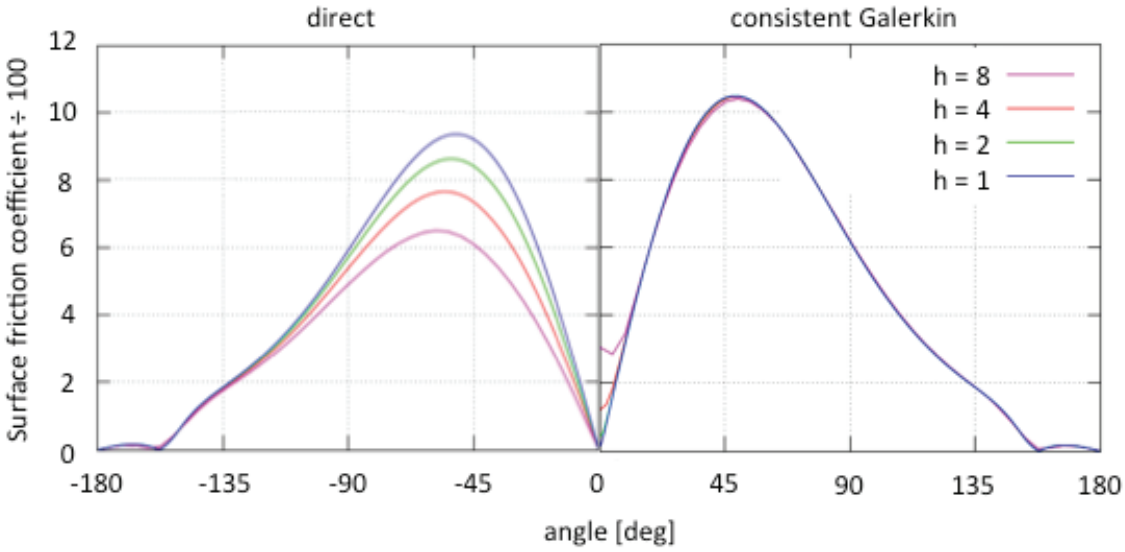

Figure 4.6. Direct approach for the surface friction coefficient (left) and Consistent Galerkin for the surface heating coefficient (right) on uniformly-refined meshes.

Chapter 5 Hypersonic Flow Over a Cylinder

The non-equilibrium boundary conditions are validated against a hypersonic / rarefied benchmark published by the Nonequilibrium Gas and Plasma Dynamics Laboratory at the University of Michigan [15].

5.1 Description of the problem

The problem studied is a hypersonic laminar flow of argon around a cylinder section at $M_\infty = 10$ for Knudsen numbers ranging from 0.01 to 0.25. The temperature of the free stream flow is 200 K and the velocity 2624 m/s. The Knudsen numbers are 0.01, 0.05 and 0.25 corresponding to densities of 2.818×10^{-5}, 5.636×10^{-6} and 1.127×10^{-6} kg/m^3, respectively. Table 5.1 reports the Knudsen, Reynolds and Mach numbers for which the simulations have been performed, with the Reynolds number computed using the diameter of the cylinder. Argon has a specific heat ratio $\gamma = 1.67$ and Prandtl number Pr = 0.667. The viscosity is modeled via the Variable Hard Sphere model, while the thermal conductivity is defined by the Eucken relation as

$$\mu = \mu_0 \left(\frac{T}{T_0} \right)^{\omega} \qquad k = \frac{9\gamma - 5}{4\gamma - 4} R\mu \tag{5.1}$$

where μ_0=5.07 × 10^{-5} kg/(m s), T_0 = 1000.0 K and ω=0.734, ω is the temperature exponent of the VHS model and R is the specific gas constant of argon, namely 208.1 J kg/K.

Kn_∞	Re	M	Regime
0.01	40	10	Continuum
0.05	80	10	Slip Regime
0.25	16	10	Transitional

Table 5.1. Values of relevant non-dimensional groups for the simulation of high speed argon flow past a cylinder.

5.1.1 Grid

The structured grid to run the simulations, shown in Figure 5.1, is based on the mesh refinement analysis of chapter 4 and consists of 252,600 nodes and 125,600 hexahedra to ensure grid independence.

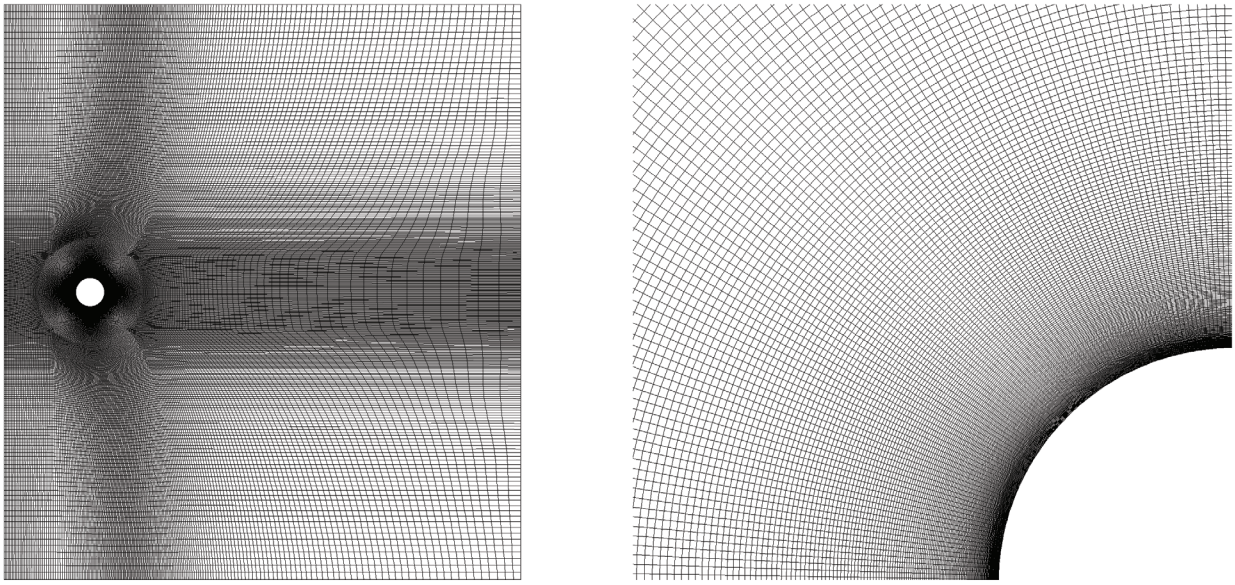

Figure 5.1. Computational mesh for the flow past a cylinder. Full grid (left), forebody close-up (right).

5.1.2 Boundary Conditions and Solver

The cylinder surface is modeled with the non-equilibrium boundary conditions described in section 3.2. Two different codes were used for the benchmark, one finite volume CFD code, LeMANS [59] and one DSMC code, MONACO [60]. The reference results are compared against HALO3D. Presently, in HALO3D, the gas is treated as a

single fluid with no chemical activity and thermal equilibrium is assumed among all energy modes such that a single temperature characterizes the flow. The following parameters are used for the 3 cases:

- AUSM^{+}UP MUSCL solver
- Van Albada shock sensor

5.2 Continuum Breakdown

In order to clearly identify the regions where non-equilibrium is occurring, a continuum breakdown parameter has been adopted. The local Knudsen number can be introduced as [22]

$$Kn_{\rho} = \lambda \left| \frac{\nabla \rho}{\rho} \right| \tag{5.2}$$

Figure 5.2 and Figure 5.3 show the continuum breakdown on the domain for the cases considered. At Kn = 0.01 and Kn = 0.05, significant non-equilibrium effects are observed in the shock, in the boundary layer and in the wake regions. At Kn = 0.25 the non-equilibrium effects are generalized through the domain and dominate the gas behavior. Figure 5.4 and Figure 5.5 present the continuum breakdown at the wall of the body, where important non-equilibrium effects can be observed in the rear part of the cylinder for Kn 0.01, 0.05 and 0.25. Note that as the Knudsen Number increases, the non-equilibrium effects do not only occupy a greater region of the domain, but their level increases as well; reaching as high as 100, well in the free-molecular flow.

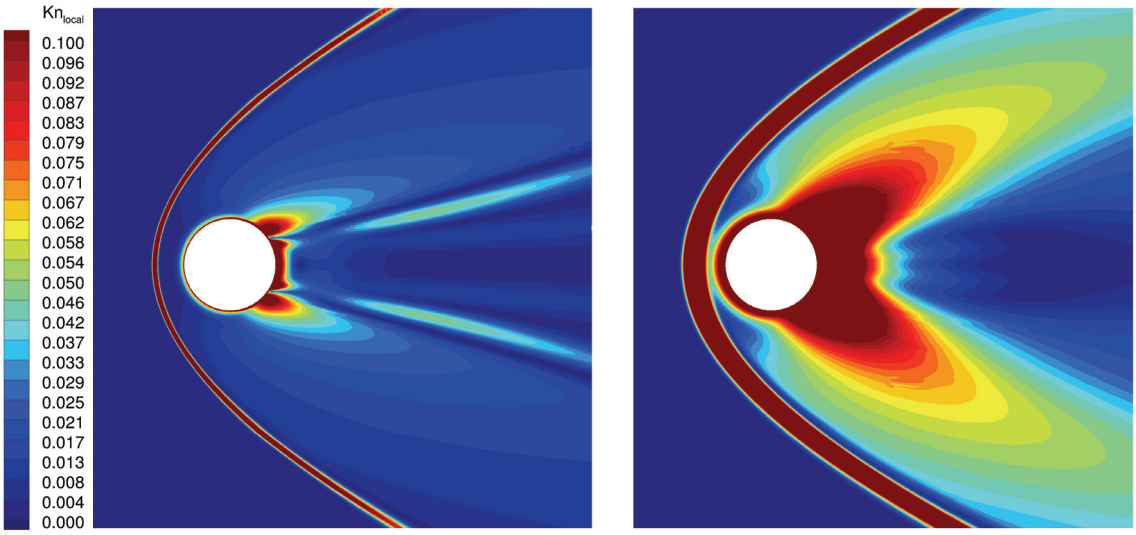

Figure 5.2 Continuum-breakdown at Kn = 0.01 (left) and Kn = 0.05 (right).

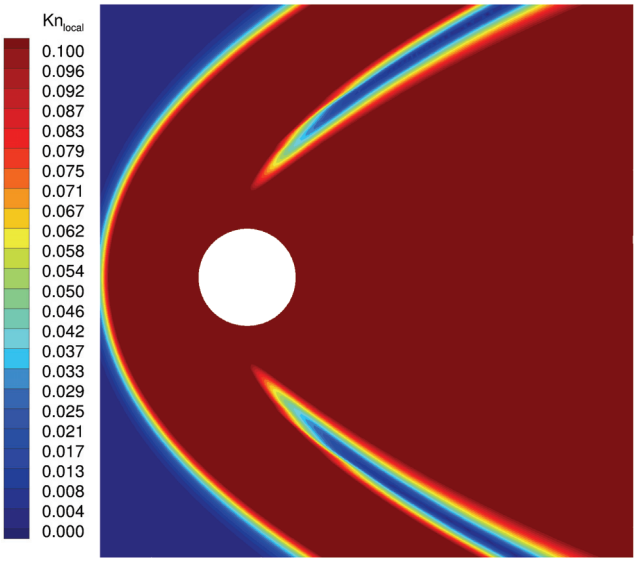

Figure 5.3. Continuum-breakdown at Kn = 0.25.

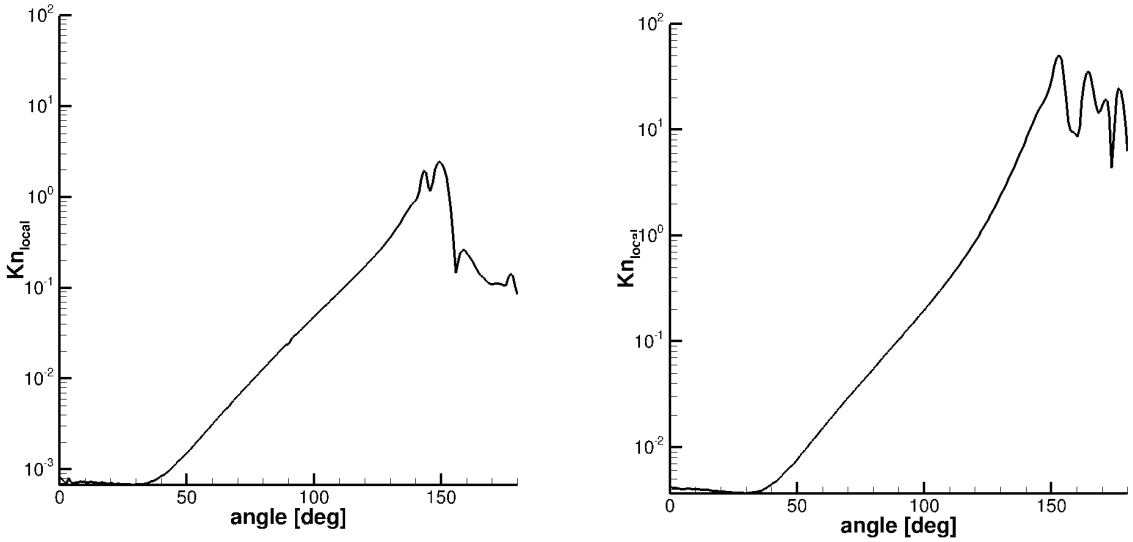

Figure 5.4, Continuum-breakdown at the wall at Kn = 0.01 (left) and Kn = 0.05 (right).

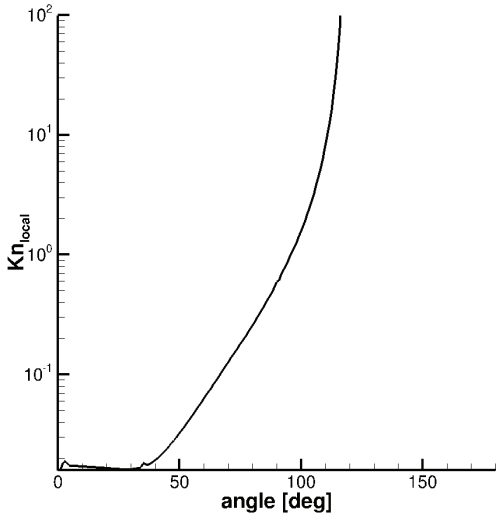

Figure 5.5. Continuum-breakdown at the wall at Kn = 0.25.

5.3 Flow Field Properties

The density and temperature fields for the three Knudsen numbers are given in Figure 5.6 to Figure 5.9. The density fields are normalized by their respective free stream value.

At Kn 0.01, the standard features of a blunt body flow are visible in the flow field properties: the bow shock detached from the body due to the high deflection angle and the high temperature region, arising from the viscous dissipation.

At higher non-equilibrium level, particularly at Kn 0.25, the shock is much more diffused and the boundary layer thickness is much larger than for higher density flows. The maximal temperature behind the shock is substantially reduced as well.

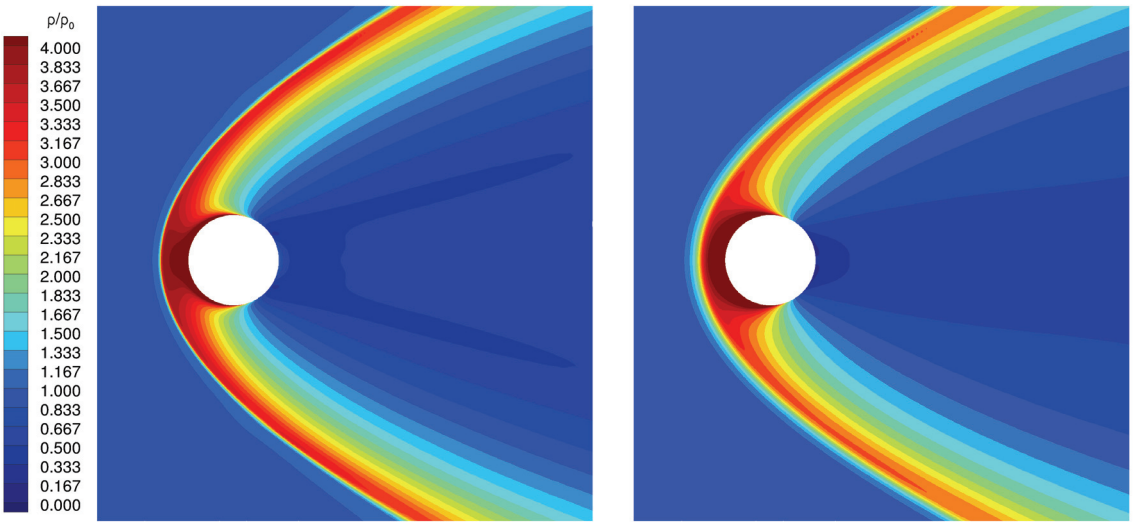

Figure 5.6. Density ratio field at Kn = 0.01 (left) and Kn = 0.05 (right).

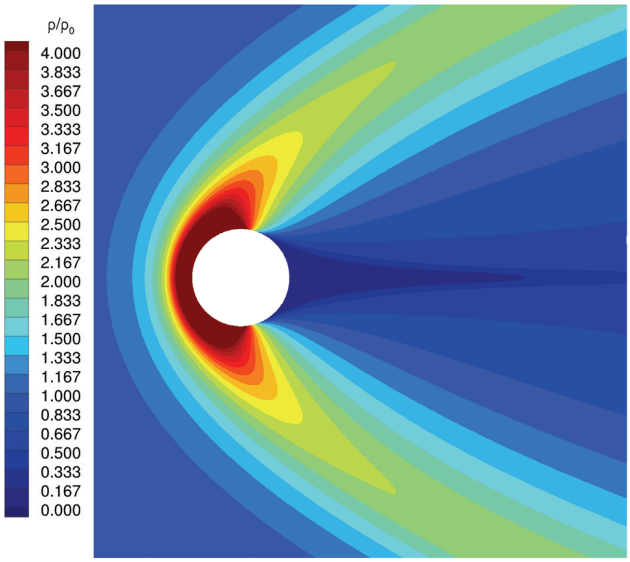

Figure 5.7. Density ratio field at Kn = 0.25.

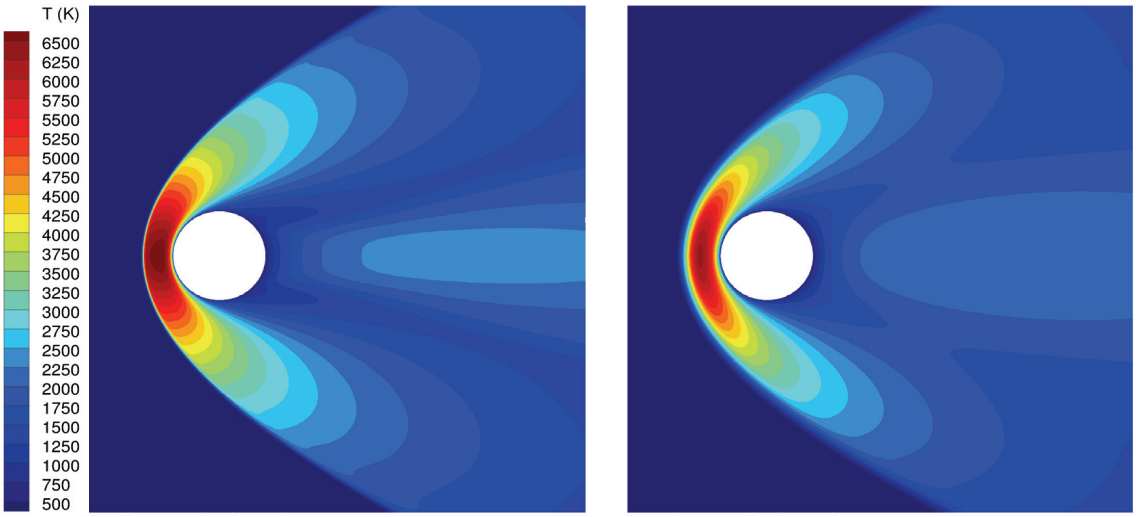

Figure 5.8. Temperature field at Kn = 0.01 (left) and Kn = 0.05 (right).

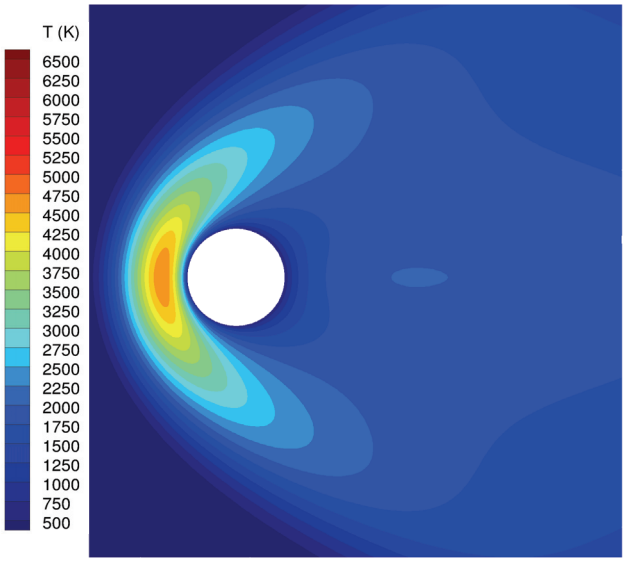

Figure 5.9 Temperature field at Kn = 0.25.

5.4 Stagnation Line

The temperature along the stagnation line is examined for the three cases (see Figure 5.10). Figure 5.11 shows the temperature profile along the stagnation line at Kn 0.01 starting at the free stream value of the flow (200 K) and instantaneously increasing due to the large amount of kinetic energy of the flow being converted to internal energy of the gas across the shock wave. It then remains constant through the shock layer and decreases to the wall value temperature as it reaches the body. At Kn 0.05, the continuum breakdown mildly affects the flow and hence the shock layer and boundary layer start to interact. Therefore, the temperature profile in Figure 5.11 (right) shows a smoother change in temperature. The same peak in temperature can still be observed. As the Knudsen number increases to Kn 0.25, the shock layer now interacts more strongly with the boundary layer. The gradient of temperature is significantly reduced as shown in Figure 5.12. The increase in the shock standoff distance can also be observed from these figures.

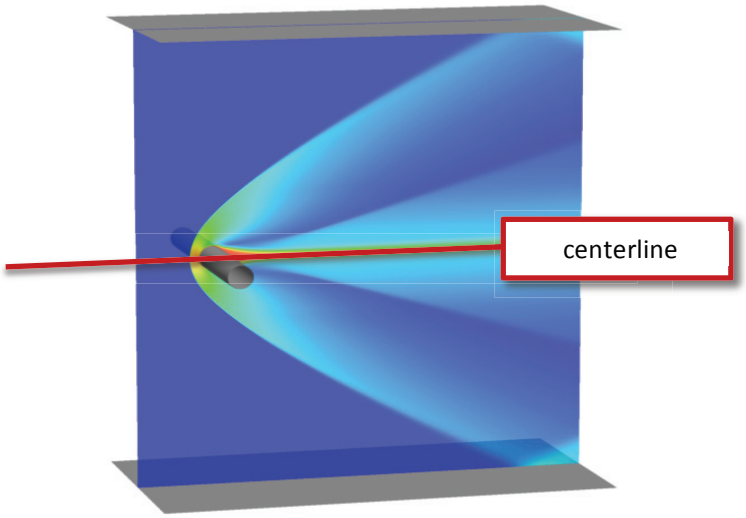

Figure 5.10. The temperature profiles are taken along the stagnation line from the inlet up to the wall.

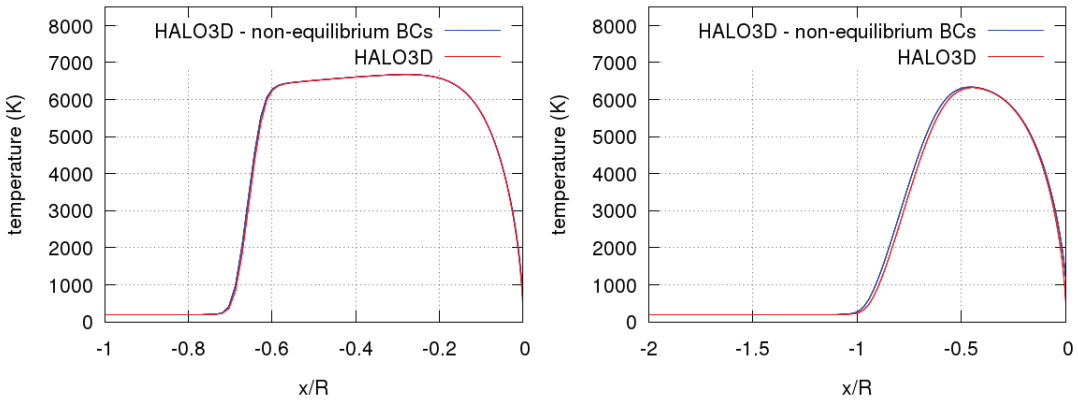

Figure 5.11. Temperature profile along the stagnation line at Kn = 0.01 (left) and Kn = 0.05 (right).

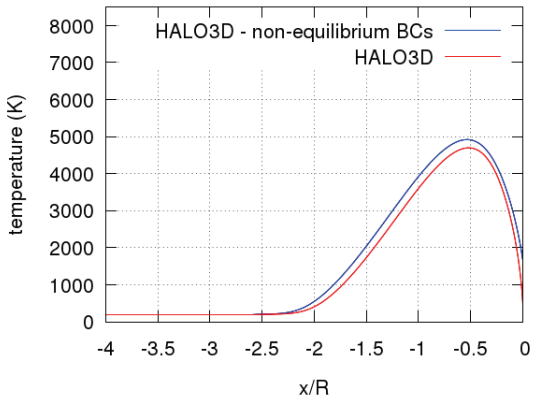

Figure 5.12. Temperature profile along the stagnation line at Kn = 0.25.

5.5 Surface Properties

Plots of surface pressure, surface heating and surface friction coefficients are presented here for the three different free stream Knudsen numbers as a function of the angle measured from the stagnation line. An angle of 0 corresponds to the front stagnation point of the cylinder and an angle of 180 is located at the rear stagnation point (Figure 5.13). The wall-related quantities are evaluated in terms of pressure, shear stress and heat flux coefficients

$$C_p = \frac{2p}{\rho_\infty U_\infty^2} \qquad C_f = \frac{2\tau}{\rho_\infty U_\infty^2} \qquad C_h = \frac{2q}{\rho_\infty U_\infty^3} \tag{5.3}$$

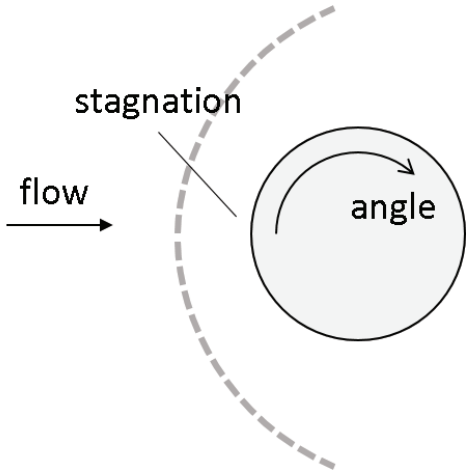

Figure 5.13. Angle location correspondence.

5.5.1 Kn = 0.01

A free-stream Knudsen number of 0.01 typically marks the end of the continuum regime and the beginning of the slip regime, where discrepancies between CFD simulations and DSMC begin to appear but are still moderate. DSMC results from [15] are used as reference data to verify the accuracy of the approach.

Figure 5.14 and Figure 5.15 compare the surface pressure, surface heating and surface friction coefficients between three different solvers: the FE HALO3D solver, the finite volume CFD code LeMANS [59] and the DSMC code MONACO [60]. Also, the solution with non-equilibrium boundary conditions is compared against the one using no-slip conditions. The curves of the surface coefficients shown in figure 5.14 and 5.15 indicate a reasonable agreement. The surface pressure coefficient matches very well over the whole surface of the cylinder. The peak heating and friction are predicted well by HALO3D. In addition, the non-equilibrium boundary conditions improve the surface heating results, especially in the rear part of the cylinder, where the results with non-equilibrium boundary conditions almost superimpose to the DSMC results. The same can be observed for the surface friction coefficient. The slip conditions improve the agreement with the DSMC solution.

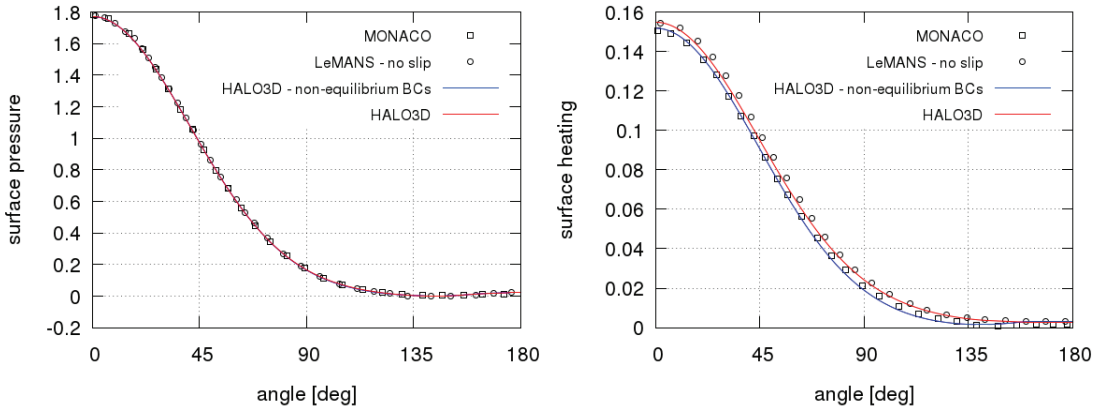

Figure 5.14. Surface pressure coefficient (left) and surface heating coefficient (right) at Kn = 0.01.

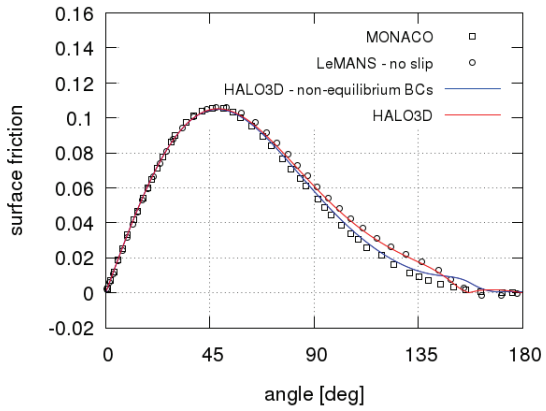

Figure 5.15. Surface friction coefficient at Kn = 0.01

5.5.2 Kn = 0.05

At a Knudsen number of 0.05, the flow is considered to be in the slip regime and the slip conditions should provide a significant improvement over the nonslip boundary conditions for the surface properties. Indeed, compared to Kn = 0.01, at Kn = 0.05, Figure 5.2 shows larger regions of continuum breakdown both in the shock and in the wake regions.

In Figure 5.16 (left), the surface pressure coefficient with or without slip boundary conditions matches very well with DSMC. It is the surface property that is the least affected by rarefaction and non-equilibrium effects. The surface heating coefficient, shown Figure 5.16 (right), on the other hand, is affected significantly by the non-equilibrium phenomena, and an improvement can be observed with the use of suitable boundary conditions. Indeed, the surface heating with the slip conditions agrees well with the DSMC solution even in a more rarefied regime particularly in the wake region. The present simulations use a standard, calorically-perfect model for argon, which could explain the slight over-prediction of the heat flux at the stagnation point compared to DSMC. As shown in Figure 5.17, the surface friction coefficients using the non-

equilibrium boundary conditions show some differences with the one obtained with DSMC. The peak magnitude and location are not perfectly captured. This could be explained in terms of the current implementation not accounting for non-equilibrium mechanisms inside the domain that can influence the dynamics of the fluid approaching the wall. As shown by comparison with LeMANS and HALO3D, the use of slip conditions yields substantial improvement with respect to DSMC.

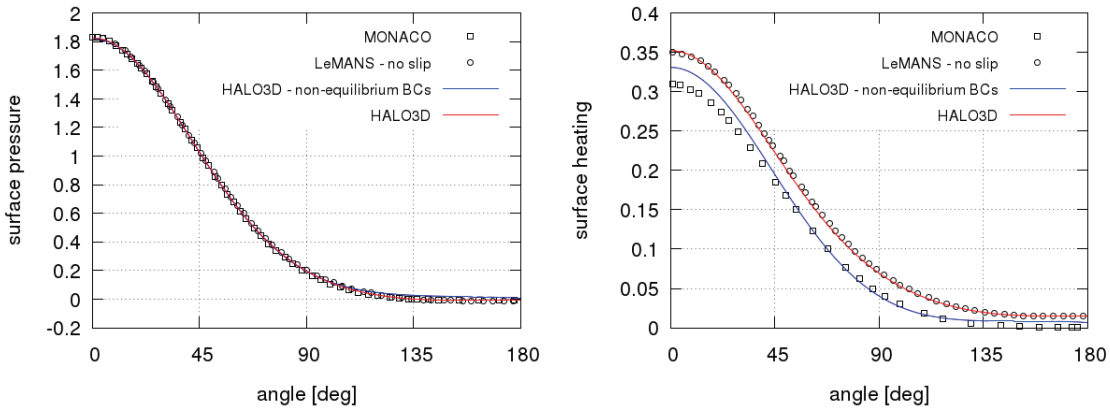

Figure 5.16. Surface pressure coefficient (left) and surface heating coefficient (right) at Kn = 0.05.

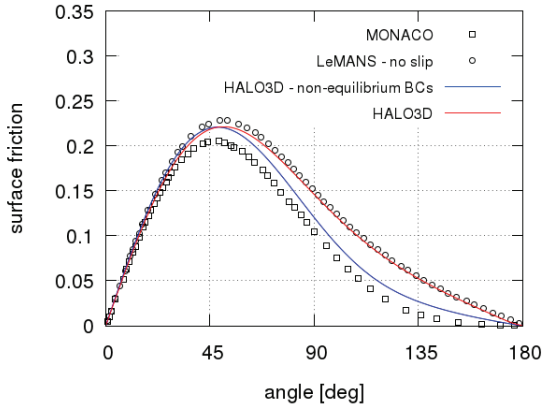

Figure 5.17. Surface friction coefficient at Kn = 0.05.

5.5.3 Kn = 0.25

At Knudsen number of 0.25, the flow is in non-equilibrium near the cylinder surface. As shown in Figure 5.5, the continuum breakdown region extends completely behind

the shock region, and the shock itself moves further away from the cylinder. Therefore, slip conditions are of paramount importance to model the gas behavior for such a high degree of rarefaction.

At this level of non-equilibrium, the surface pressure coefficients are now slightly affected. Indeed, Figure 5.18 (left) shows surface pressure coefficient that does not match DSMC at the stagnation point and in the wake region. As shown in Figure 5.18 (right) the surface heating coefficient predicted by HALO3D does not compare well with the DSMC simulation, despite the significant improvement with respect to the other continuum-based methods. The same can be said for the surface friction coefficient, shown in Figure 5.19. In the transition regime, non-equilibrium boundary conditions are not enough to account for the level of rarefaction as it can be seen from these results.

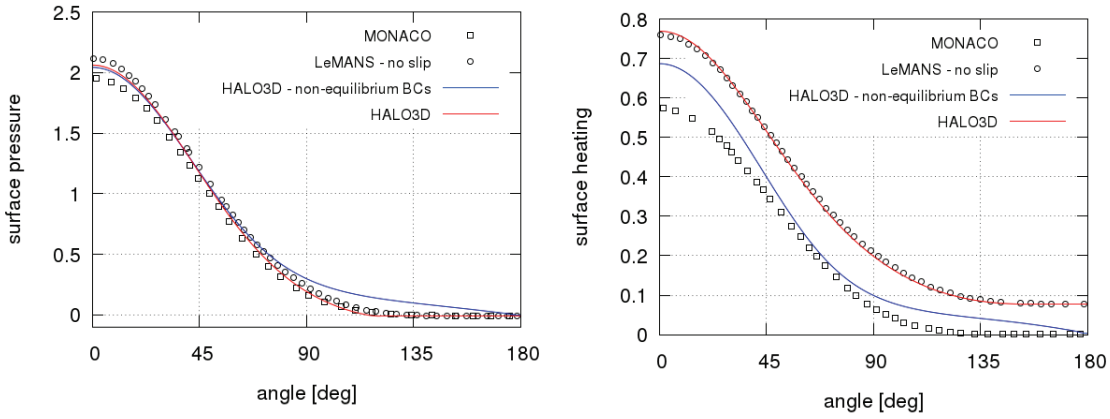

Figure 5.18. Surface pressure coefficient (left) and surface heating coefficient (right) at Kn = 0.25.

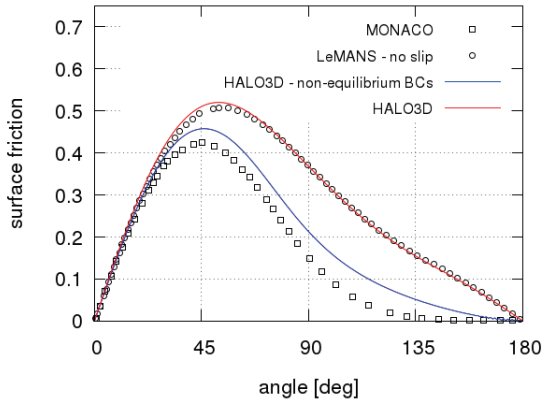

Figure 5.19 Surface friction coefficient at Kn = 0.25.

5.6 Slip Quantities

Here, the effects of the continuum breakdown on the velocity slip and temperature jump are investigated. Figure 5.20 on the left presents the velocity as a function of the angle measured from the stagnation line while Figure 5.20, right, shows the temperature jump as a function of the angle, where the initial temperature on the cylinder was fixed at 500 K. The salient feature of these slip quantities is the increase in the values of the jump as the non-equilibrium phenomena becomes more significant.

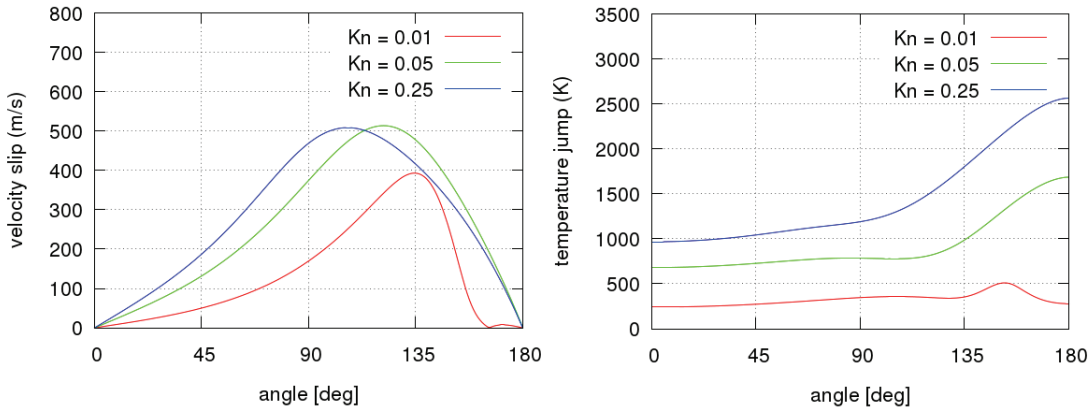

Figure 5.20. Velocity slip (left) and temperature jump (right) at Kn = 0.01, 0.05 and Kn = 0.25

5.7 Difference in Drag and Peak Heating

The integrated drag and peak heating are provided in Table 5.2 and Table 5.3 respectively. These tables show the values predicted by DSMC and CFD with non-equilibrium slip conditions as well as without slip conditions. Note that the no-slip conditions here refer to an isothermal wall with fixed temperature at 500 K and a no-slip velocity condition on the surface of the cylinder (V = 0 m/s). The percentage difference given in the last column is calculated between the no-slip and the slip values. The DSMC results are provided as a reference. At Kn = 0.01, the integrated drag and peak heating agree very well between the no-slip and slip conditions. However, the agreement diminishes with increasing Knudsen number. At the highest Knudsen number, the total drag exhibits a difference from the DSMC results as high as 15% and 12% for the peak heating. Nonetheless, it can be observed that the presence of slip conditions improves the agreement with DSMC for all the flow regimes investigated.

A reduced drag and heat on the re-entry phase of hypersonic vehicles has a tremendous impact. Flying with a lower drag affects the reduction in speed / Mach that the vehicle is able to achieve. This could affect the trajectory of the vehicle and the final speed and angle the vehicle will have to maintain for a safe landing. Similarly, with a reduced heat, the re-entry vehicle could be allowed to have a lighter TPS or use a material that has better mechanical properties.

Kn_∞	DSMC	No-slip	Slip	% Difference
0.01	40.02	38.90	38.86	0.08
0.05	8.866	9.07	8.74	3.85
0.25	2.092	2.49	2.16	15.33

Table 5.2. Drag/unit span (N/m) difference from the no-slip results and the non-equilibrium slip results.

Kn_∞	DSMC	No-slip	Slip	% Difference
0.01	39.13	39.42	38.64	2.011
0.05	15.85	17.93	16.85	6.411
0.25	5.926	7.833	6.992	12.02

Table 5.3. Peak heating (kW/m^2) difference from the no-slip results and the non-equilibrium slip results.

Chapter 6 Hypersonic Flow over a Sphere

This chapter considers the hypersonic flow past a sphere. As the previous chapter was on a 2D problem with a monoatomic gas, this study extends the assessment to a 3D blunt geometry with a diatomic gas [49].

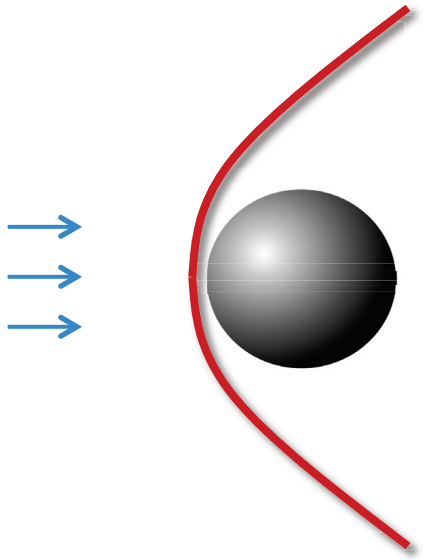

Figure 6.1. Mach 10 flow of nitrogen over a sphere.

6.1 Description of the Problem

The non-equilibrium boundary conditions are validated on a hypersonic laminar flow of nitrogen, past a sphere. The mesh for this case is made of 3,116,727 elements and 938,763 nodes (Figure 6.2) with proper refinement for resolution of the detached bow shock and viscous boundary layer. The flow conditions are summarized in Table 6.1 and Table 6.2. Nitrogen has a specific heat ratio γ = 1.4, Prandtl number Pr= 0.7368 and gas constant R = 296.8 J kg/K. The VHS model of Eq. 5.1 is used with μ_0=1.67 × 10^{-5} kg/(m s), T_0 = 273.0 K and ω=0.75. R in this case, is the specific gas constant of nitrogen. The results are taken through the symmetry plane of the sphere.

Velocity	2884 m/s
Mach number	10
Free stream	200 K

Table 6.1. Flow properties for the flow of nitrogen over a sphere at Mach 10.

ρ_∞	Pressure	Kn_∞	Re_∞
1.975×10^{-5} kg/m^3	1.17 Pa	0.01	1280
3.949×10^{-6} kg/m^3	0.23 Pa	0.05	256
7.899×10^{-7} kg/m^3	0.047 Pa	0.25	51.2

Table 6.2. Simulated regimes for the flow of nitrogen over a sphere.

6.1.1 Boundary Conditions and Solver

As with the cylinder, the surface of the sphere is modeled with the non-equilibrium boundary conditions presented in section 3.2. The same codes, namely the DSMC code, MONACO [60] and LeMANS [59], are used as a reference to compare with HALO3D.

The following parameters are used for the three flow regimes:

- AUSM$^+$UP MUSCL solver
- Van Albada shock sensor

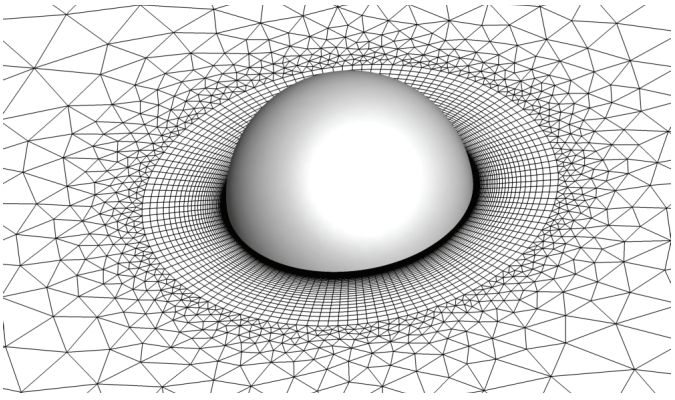

Figure 6.2. Computational mesh for the flow past a sphere.

6.2 Continuum Breakdown

As shown in Figure 6.3, at Kn = 0.01, non-equilibrium effects are present in the shock, boundary layer and wake regions. Although this global Knudsen number is not commonly associated with a fully rarefied flow, local regions of breakdown appear where the flow behaves in a rarefied manner and require a special treatment for the near-wall region. At a global Kudsen number of 0.05, the non-equilibrium regions become more important as seen in Figure 6.3. At Kn = 0.25, the treatment of the continuum breakdown effects is critical. Figure 6.4 shows the gradient length Knudsen number where the flow is almost entirely in non-equilibrium.

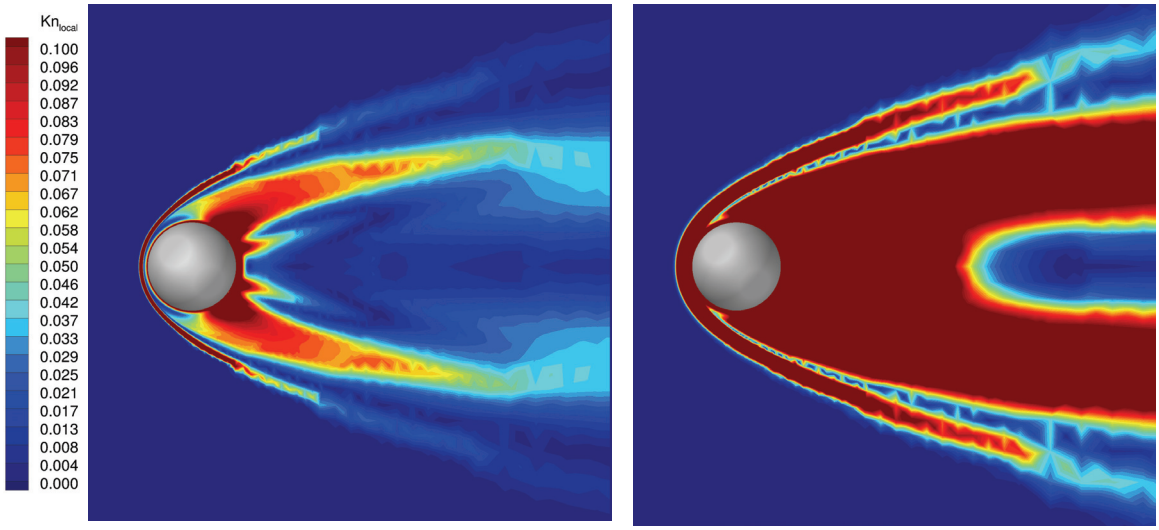

Figure 6.3. Continuum-breakdown at Kn = 0.01 (left) and Kn = 0.05 (right).

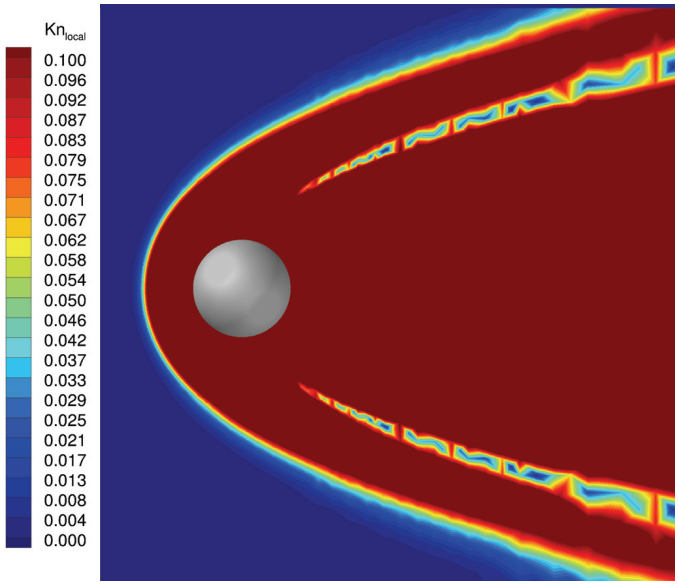

Figure 6.4. Continuum-breakdown at Kn = 0.25.

6.3 Flow Field Properties

This section presents the normalized density ratio field as well as the temperature field. Figure 6.5 shows the density field at Kn 0.01 (left) and Kn0.05 (right), while Figure 6.6 shows the density field at Kn 0.25. As with the cylinder, the standard features of a blunt body flow are observed. Note here, that the shock standoff distance is reduced compared to the cylinder. Nonetheless, as the Knudsen number increases, the shock becomes much more diffuse.

The temperature field at Kn 0.01, Kn 0.05 and Kn 0.25 are given in Figure 6.7 and Figure 6.8. These figures show that the peak temperature occurring in front of the sphere is much lower than for the cylinder. It is around 4000 K, which is not enough to cause significant dissociation of the nitrogen molecules as dissociation starts to take place between 3500 K and 6000 K.

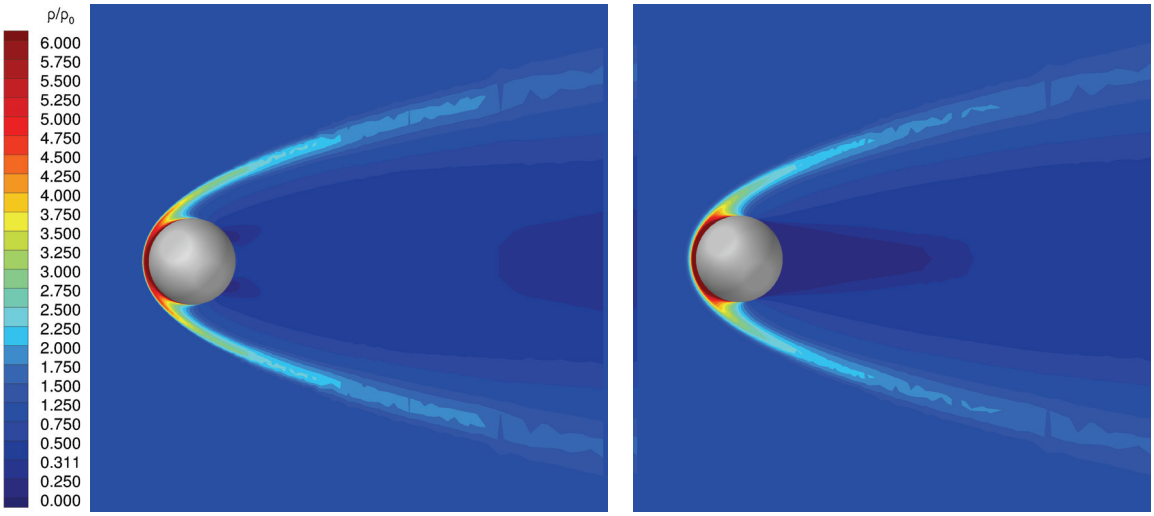

Figure 6.5. Density ratio field at Kn = 0.01 (left) and Kn = 0.05 (right).

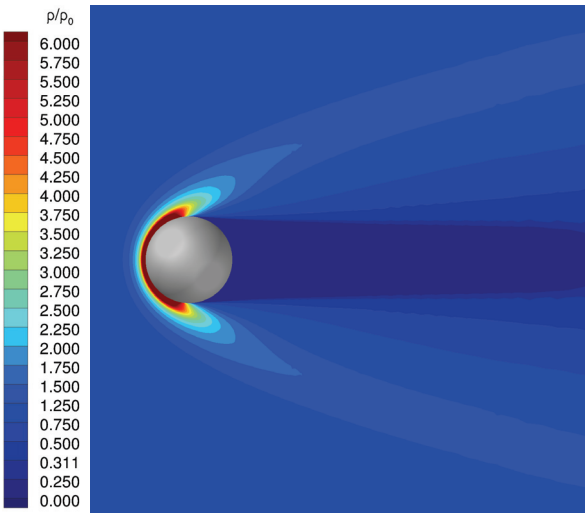

Figure 6.6. Density ratio field at Kn = 0.25.

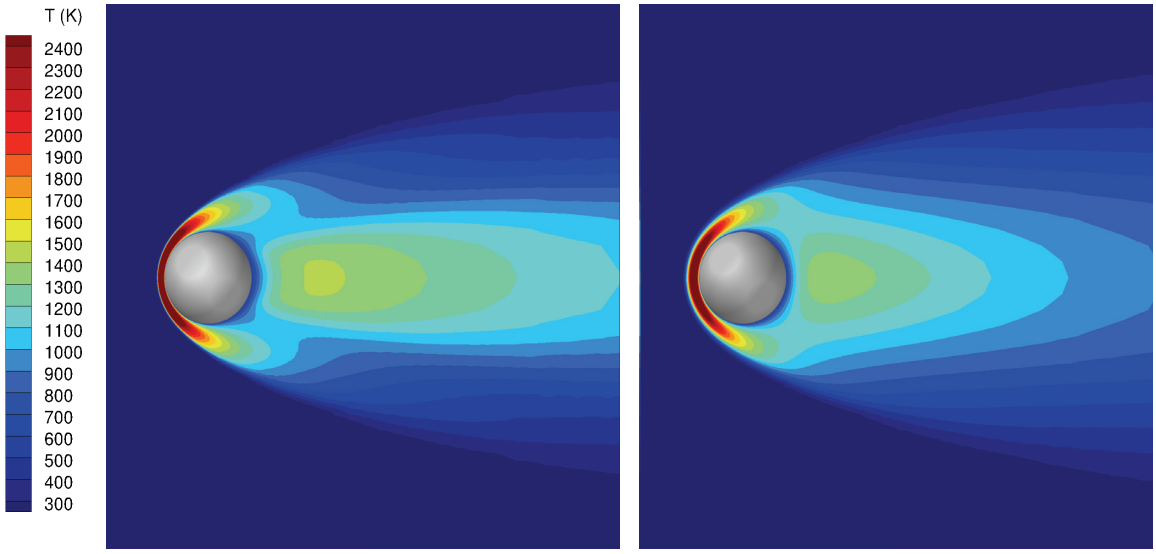

Figure 6.7. Temperature field at Kn = 0.01 (left) and Kn = 0.05 (right).

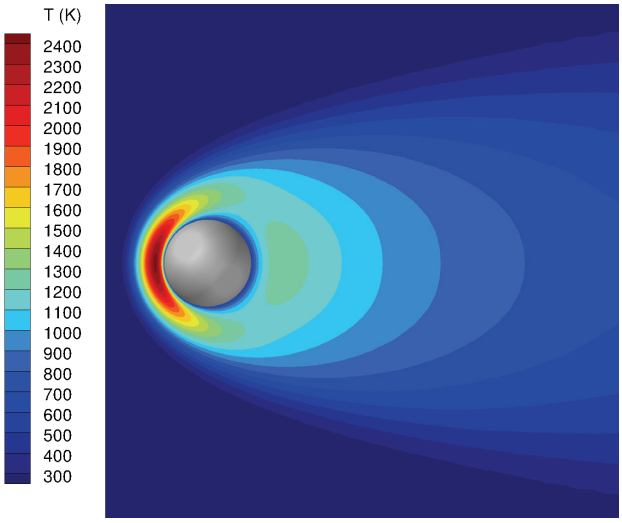

Figure 6.8. Temperature field at Kn = 0.25.

6.4 Surface Properties

In this section, the effects of non-equilibrium on the surface properties of the sphere are investigated.

6.4.1 Kn = 0.01

Figure 6.9 shows the comparison of the surface pressure and surface heating coefficients taken at the symmetry plane of the sphere with the solutions obtained with LeMANS, MONACO and HALO3D. The agreement between the solvers is very good for the surface pressure, but a small difference is apparent near the stagnation point. The peak heating (right) is over-predicted in the solution with slip conditions. The slip boundary condition compares better with DSMC than the no-slip conditions solutions in terms of heat flux. Note however, that DSMC includes variable vibrational and rotational energy exchange models, whereas HALO3D currently does not. For the surface friction (Figure 6.10), the temperature jump and velocity slip improve considerably the agreement with DSMC, particularly in the wake region but also near the peak.

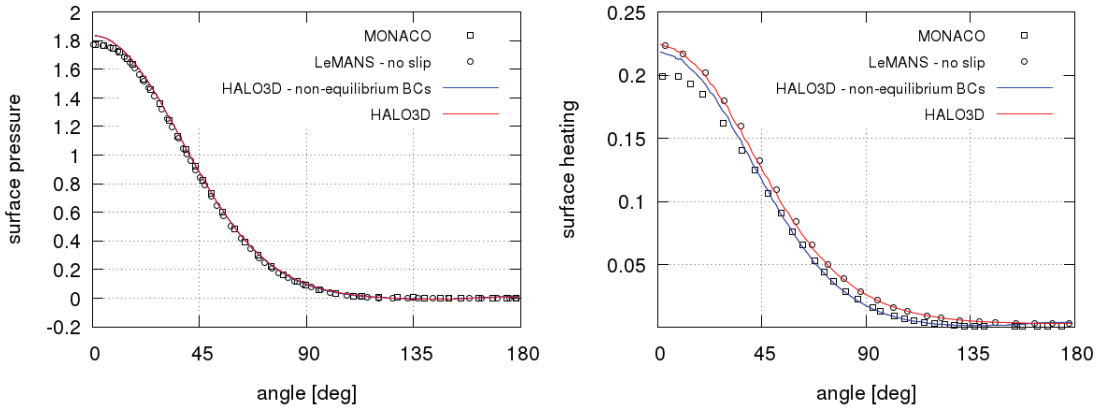

Figure 6.9. Surface pressure coefficient (left) and surface heating coefficient (right), at Kn = 0.01.

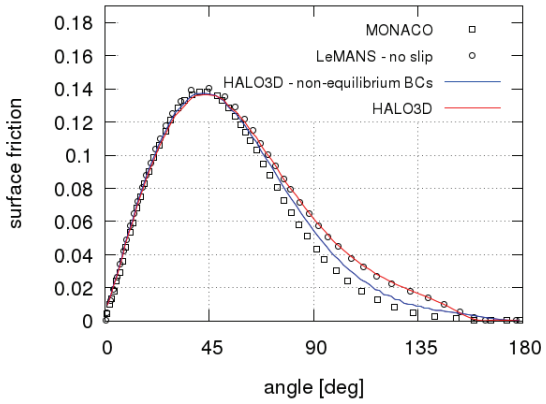

Figure 6.10. Surface friction coefficient at Kn = 0.01.

6.4.2 Kn = 0.05

Figure 6.11 shows that the surface pressure and surface heating coefficients. The agreement between the different solvers is very good for the surface pressure coefficient. The surface heating is over-predicted by HALO3D over the sphere. With the non-equilibrium boundary conditions, the heat flux is slightly under-predicted at the stagnation point. The surface friction coefficient does not match well with the DSMC simulation shown in Figure 6.12. The peak friction coefficient location has moved slightly further on the sphere with the non-slip conditions. However, the agreement with DSMC for the wake region improves with the non-equilibrium boundary conditions. Overall, the proposed slip conditions improve the prediction of shear stress and heat flux, particularly in the wake region.

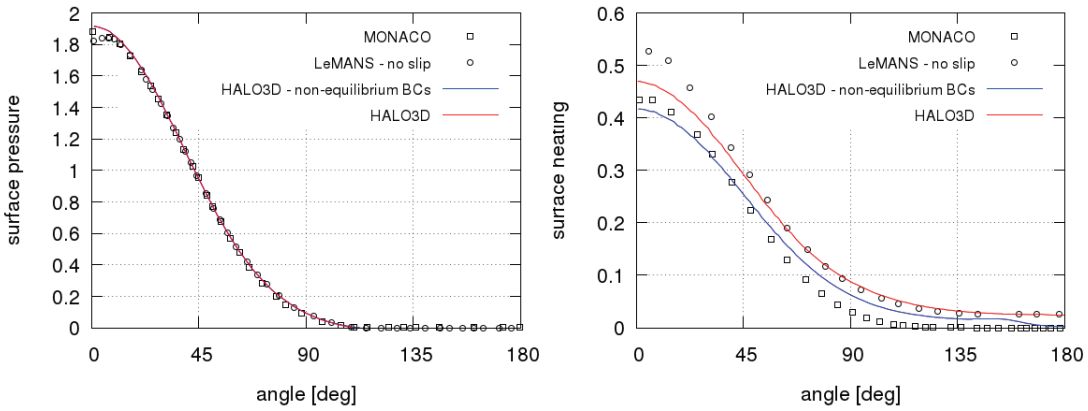

Figure 6.11. Surface pressure coefficient (left) and surface heating coefficient (right), at Kn = 0.05.

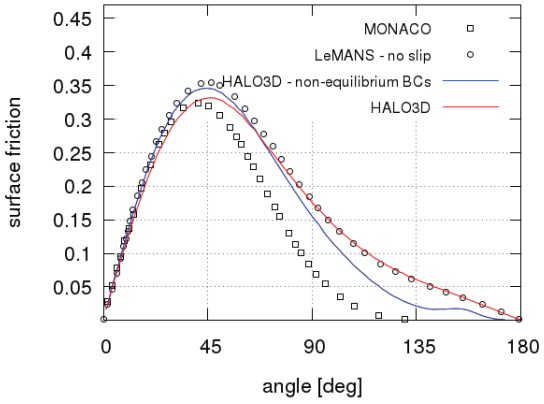

Figure 6.12. Surface friction coefficient at Kn = 0.05.

6.4.3 Kn = 0.25

Figure 6.13 (left) presents the surface pressure coefficient that is over-predicted at the stagnation point. Figure 6.13 (right) and Figure 6.14 show the surface heating and friction coefficients where the various solvers are no longer in agreement. HALO3D with or without slip conditions overestimate both surface properties with respect to DSMC near the fore body of the sphere. The heat flux and shear stress show large differences between the DSMC solver and the FE CFD solver. At this Knudsen number, the slip conditions are not solely sufficient to address the continuum breakdown. More sophisticated strategies are required. Nonetheless, the slip conditions yield an

improvement in the heat flux prediction. The same can be said for the surface shear stress, where, even though the differences between DSMC and HALO3D are still important, the differences are minimized with the slip conditions.

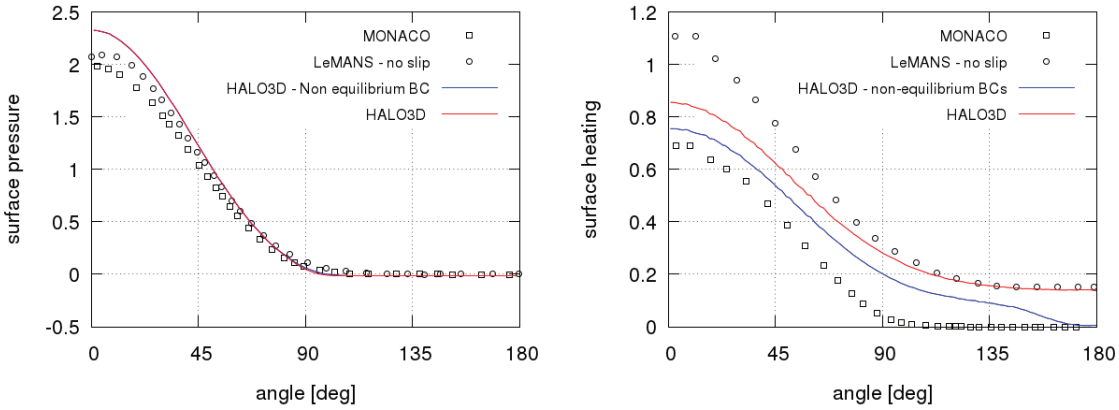

Figure 6.13. Surface pressure coefficient (left) and surface heating coefficient (right), at Kn = 0.25.

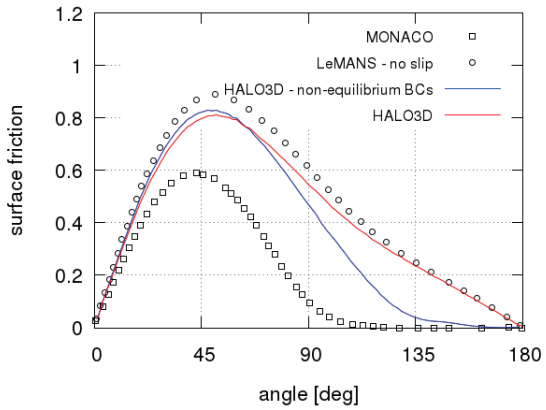

Figure 6.14. Surface friction coefficient at Kn = 0.25.

6.5 Slip Quantities

The temperature jump and velocity slip can be seen in Figure 6.15 for the three Knudsen number investigated. The initial temperature on the sphere was fixed to 500 K. As with the cylinder, the same behavior is noted: as the Knudsen number increases, the value of the jump in field variables also increases.

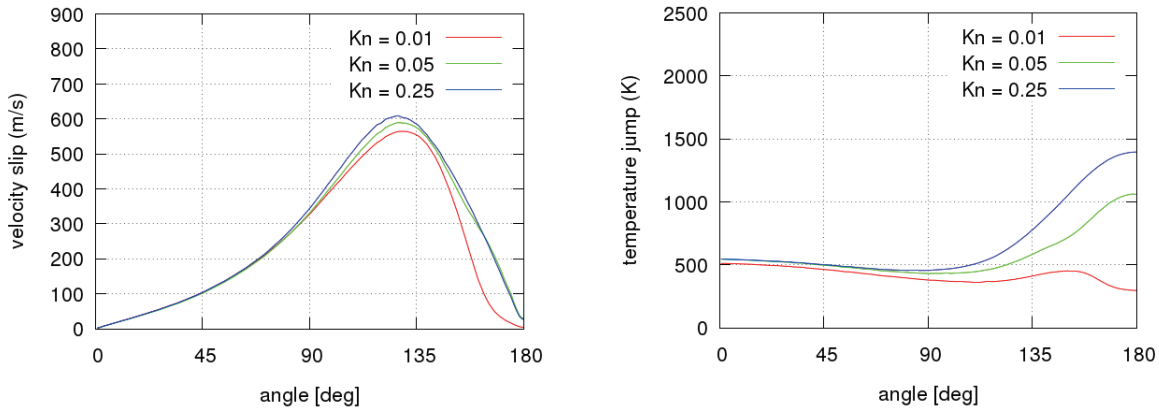

Figure 6.15. Velocity slip (left) and temperature jump (right) at Kn = 0.01, 0.05 and Kn = 0.25.

Chapter 7 Conclusions

7.1 Summary and Contributions

The purpose of this research was to formulate a FE-based approach to improve the modeling of the non-equilibrium physics in the vicinity of the surface of the vehicle allowing to address flows in the slip / transitional regime.

To do so, a Consistent Galerkin Finite Element method was proposed to compute wall boundary conditions in the non-equilibrium regime to second order accuracy. The method relies on the low-cost re-evaluation of both the momentum and energy equations using previously computed integrals. The order of convergence of the methodology was confirmed via a grid-refinement analysis where the robustness of the methodology was demonstrated in the presence of shocks.

Tests were performed on a cylinder and a sphere at very high speeds in regimes ranging from continuum to transitional and showed the advantages of the proposed methodology, as well as some of its remaining limitations and issues. The results showed that at large Knudsen number, the differences in aerothermodynamic properties between CFD and DSMC are significant, highlighting the necessity to have non-equilibrium boundary conditions to address the breakdown of the assumption of continuity in the N-S equations. For all simulations, however, agreement with DSMC was improved with the more accurate slip conditions, particularly in the wake of the two geometries. Nevertheless, from the results, it is also clear that boundary conditions by themselves are insufficient to model accurately high-Mach / rarefied regimes.

7.2 Future Work

Geometry

The current study investigated extensively blunt bodies in 2D and 3D. Further studies should be performed on sharp geometries as these are characterized by an attached shock and supersonic velocities throughout the flow and hence, important differences are expected in terms of non-equilibrium and surface properties.

Thermal non-equilibrium

A next step for the development would be to model high-temperature effects. This requires introducing additional equations to the system to account for rotational and vibrational energy modes that are activated at high-temperature.

Gas mixtures

The study was limited to argon and nitrogen. To model hypersonic flows in a more representative manner; it is necessary to consider multi-species flow. Air is a mixture of nitrogen (N_2), oxygen (O_2), argon (Ar), carbon dioxide (CO_2), Neon (Ne) and some traces of other components. At a negligible ionization level, a five species mixture (O_2, N_2, NO, O, N) can accurately represent air, but at high temperatures, the air composition is drastically changed and an eleven species mixture is required to model real gas effect.

Rarefied gas dynamics

A suitable formulation of the Bhatnagar-Gross-Krook kinetic scheme within the finite element framework could extend the applicability of the macroscopic approach up to values of the Knudsen number in the order of unity. This would not only allow for the development of a unified approach to solve rarefied/high Mach problems in an efficient

manner but the edge based formulation facilitates the development of an approach that can capture domain of arbitrary topology, as well in an efficient manner. Eventually it will be necessary to account for the coupling between continuum and molecular approaches, i.e. N-S and DSMC methods.

Bibliography

[1] J. D. Anderson, *Hypersonic and High-Temperature Gas Dynamics*: American Institute of Aeronautics and Astronautics, 1989.

[2] J. Moss, K. Boyles, and F. Greene, "Orion Aerodynamics for Hypersonic Free Molecular to Continuum Conditions," *14th AIAA/AHI Space Planes and Hypersonic Systems and Technologies Conference*, International Space Planes and Hypersonic Systems and Technologies Conferences: American Institute of Aeronautics and Astronautics, 2006.

[3] S. Berry, R. Kimmel, and E. Reshotko, "Recommendations for Hypersonic Boundary Layer Transition Flight Testing," *41st AIAA Fluid Dynamics Conference and Exhibit*, Fluid Dynamics and Co-located Conferences: American Institute of Aeronautics and Astronautics, 2011.

[4] G. Tchuen, and Y. Burtschell, "Physico - Chemical Modelling in Nonequilibrium Hypersonic Flow Around Blunt Bodies," *Aeronautics and Astronautics*, P. M. Mulder, ed. InTech, 2011.

[5] *Code of Federal Regulations, Part 431, Launch and Reentry of a Reusable Launch Vehicle (RLV)* F. A. Administration.

[6] *AC-431.35-2A, Reusable Launch and Reentry Vehicle System Safety Process* F. A. Administration, 2005.

[7] L. Gong, S. Zhang, P. Tang *et al.*, “Implication of Mishaps to Preliminary Hazard Analysis of Hypersonic Vehicles,” *Procedia Engineering,* vol. 80, pp. 437-444, 2014/01/01, 2014.

[8] T. Malik. "Death of DARPA's Superfast Hypersonic Glider Explained," http://www.space.com/15388-darpa-hypersonic-glider-demise-explained.html.

[9] D. P. Affairs, “Engineering Review Board Concludes Review of HTV-2 Second Test Flight,” 2012.

[10] C. Miller, "Aerothermodynamic flight simulation capabilities for aerospace vehicles," *20th AIAA Advanced Measurement and Ground Testing Technology Conference*, Fluid Dynamics and Co-located Conferences: American Institute of Aeronautics and Astronautics, 1998.

[11] D. Vennemann, “Hypersonic Test Facilities Available in Western Europe for Aerodynamic/Aerothermal and Structure/Material Investigations,” *Philosophical Transactions: Mathematical, Physical and Engineering Sciences,* vol. 357, no. 1759, pp. 2227-2248, 1999.

[12] G. S. R. Sarma, “Physico chemical modelling in hypersonic flow simulation,” *Progress in Aerospace Sciences,,* vol. 36, no. 3, pp. 281-349.

[13] L. Trimmer, J. A. Cary, and R. Voisinet, "The optimum hypersonic wind tunnel," *14th Aerodynamic Testing Conference*, Aerodynamic Testing Conference: American Institute of Aeronautics and Astronautics, 1986.

[14] T. C. Lin, “Influence of Laminar Boundary-Layer Transition on Entry Vehicle Designs,” *Journal of Spacecraft and Rockets,* vol. 45, no. 2, pp. 165-175, 2008/03/01, 2008.

[15] A. J. Lofthouse, “Non-equilibrium Hypersonic Aerothermodynamics Using the Direct Simulation Monte Carlo and Navier-Stokes Models,” PhD Thesis, University of Michigan, 2008.

[16] J. F. Wendt, and J. M. Muylaert, “Status of Hypersonic Testing Capabilities in Europe,” *2nd European ESA Symposium Proceedings*, pp. 165-172, 1995.

[17] D. J. Quattrochi, “Hypersonic Heat Transfer and Anisotropic Visualization with a Higher Order Discontinuous Galerkin Finite Element Method,” Master Thesis, Massachusetts Institute of Technology, 2006.

[18] P. M. Gresho, “Some Current CFD Issues Relevant to the Incompressible Navier-Stokes Equations, ” *Computer Methods in Applied Mechanics and Engineering*, vol 87, no 2, pp. 201-252, 1991.

[19] P. M. Gresho, R. L. Lee, R. L. Sani *et al.*, “The Consistent Galerkin FEM for Computing Derived Boundary Quantities in Thermal and or Fluids Problems,” *International Journal for Numerical Methods in Fluids,* vol. 7, no. 4, pp. 371-394, 1987.

[20] W. G. Vincenti, and C. H. Kruger, “Introduction to physical gas dynamics. 1965,” *New Yor: Wiley*.

[21] A. J. Lofthouse, L. C. Scalabrin, and I. D. Boyd, “Velocity Slip and Temperature Jump in Hypersonic Aerothermodynamics,” *Journal of Thermophysics and Heat Transfer,* vol. 22, no. 1, pp. 38-49, 2008.

[22] I. D. Boyd, “Predicting Breakdown of the Continuum Equations Under Rarefied Flow Conditions,” *AIP Conference Proceedings,* vol. 663, no. 1, pp. 899-906, 2003.

[23] M. Gad-el-Hak, “The fluid mechanics of microdevices-the Freeman scholar lecture,” *Transactions-American Society of Mechanical Engineers Journal of Fluids Engineering,* vol. 121, pp. 5-33, 1999.

[24] L. L. Baker, “Efficient numerical methods for solving the Boltzmann equation for small scale flows,” PhD Thesis, Massachusetts Institute of Technology, 2007.

[25] G. A. Bird, *Molecular Gas Dynamics and the Direct Simulation of Gas Flows*: Oxford University Press, 1994.

[26] W.-L. Wang, and I. D. Boyd, “Predicting continuum breakdown in hypersonic viscous flows,” *Physics of Fluids,* vol. 15, no. 1, pp. 91-100, 2003.

[27] W.-L. Wang, and I. D. Boyd, “Hybrid DSMC-CFD Simulations of Hypersonic Flow over Sharp and Blunted Bodies, “ *36th AIAA Thermophysics Conference*, Fluid Dynamics and Co-located Conferences: American Institute of Aeronautics and Astronautics, 2003.

[28] W.-L. Wang, Q. Sun, and I. D. Boyd, “Towards Development of a Hybrid DSMC-CFD Method for Simulating Hypersonic Interacting Flows,” *8th AIAA/ASME Joint Thermophysics and Heat Transfer Conference*, Fluid Dynamics and Co-located Conferences: American Institute of Aeronautics and Astronautics, 2002.

[29] H. Carlson, R. Roveda, I. D. Boyd *et al.*, “A Hybrid CFD-DSMC Method of Modeling Continuum-Rarefied Flows, ” *42nd AIAA Aerospace Sciences Meeting and Exhibit*, Aerospace Sciences Meetings: American Institute of Aeronautics and Astronautics, 2004.

[30] J. M. Burt, and I. D. Boyd, “A Hybrid Particle Approach for Continuum and Rarefied Flow Simulation,” *Journal of Computational Physics,* vol. 228, no. 2, pp. 460-475, 2009.

[31] T. Schwartzentruber, and I. D. Boyd, “Detailed Analysis of a Hybrid CFD-DSMC Method for Hypersonic Non-Equilibrium Flows,” *38th AIAA Thermophysics*

Conference, Fluid Dynamics and Co-located Conferences: American Institute of Aeronautics and Astronautics, 2005.

[32] A. Guardone, and L. Quartapelle, “Unstructured finite-volume high-resolution methods for conservation laws.” Available from: http://services.aero.polimi.it/~quartape/bacheca/materiale_didattico/driver.pdf.

[33] J. Padilla, and I. Boyd, "Assessment of Gas-Surface Interaction Models in DSMC Analysis of Rarefied Hypersonic Flow," *39th AIAA Thermophysics Conference*, Fluid Dynamics and Co-located Conferences: American Institute of Aeronautics and Astronautics, 2007.

[34] W.-M. Zhang, G. Meng, and X. Wei, “A review on slip models for gas microflows,” *Microfluidics and Nanofluidics,* vol. 13, no. 6, pp. 845-882, 2012.

[35] R. I. Masel, *Principles of adsorption and reaction on solid surfaces*: John Wiley & Sons, 1996.

[36] T. Gökçen, and R. W. MacCormack, “Nonequilibrium Effects for Hypersonic Transitional Flows Using Continuum Approach,” *27th Aerospace Sciences Meeting*, Aerospace Sciences Meetings: American Institute of Aeronautics and Astronautics, 1989.

[37] D. A. Lockerby, J. M. Reese, D. R. Emerson *et al.*, “Velocity Boundary Condition at Solid Walls in Rarefied Gas Calculations,” *Physical Review,* vol. 70, no. 1, 2004.

[38] C. J. Greenshields, and J. M. Reese, “Rarefied Hypersonic Flow Simulations Using the Navier–Stokes Equations with Non-equilibrium Boundary Conditions,” *Applied Computational Aerodynamics and High Performance Computing in the UK,* vol. 52, pp. 80-87, 2012.

[39] J. C. Maxwell, “On Stresses in Rarified Gases Arising from Inequalities of Temperature,” *Philosophical Transactions of the Royal Society of London,* vol. 170, pp. 231-256, 1879.

[40] M. Fossati, A. Guardone, L. Vigevano *et al.*, “Kinetic Node-Pair Formulation for Two-Dimensional Flows from Continuum to Transitional Regime,” *AIAA Journal,* vol. 51, no. 4, pp. 784-796, 2013.

[41] D. A. Lockerby, J. M. Reese, and M. A. Gallis, “Capturing the Knudsen Layer in Continuum-Fluid Models of Nonequilibrium Gas Flows,” *AIAA Journal,* vol. 43, no. 6, pp. 1391-1393, 2005.

[42] N. T. P. Le, C. White, J. M. Reese *et al.*, “Langmuir–Maxwell and Langmuir–Smoluchowski Boundary Conditions for Thermal Gas Flow Simulations in Hypersonic Aerodynamics,” *International Journal of Heat and Mass Transfer,* vol. 55, no. 19–20, pp. 5032-5043, 2012.

[43] S. H. Kim, H. Pitsch, and I. D. Boyd, “Slip Velocity and Knudsen Layer in the Lattice Boltzmann Method for Microscale Flows,” *Physical Review,* vol. 77, no. 2, 2008.

[44] Q. Li, S. Fu, and K. Xu, “Application of Gas-Kinetic Scheme with Kinetic Boundary Conditions in Hypersonic Flow,” *AIAA Journal,* vol. 43, no. 10, pp. 2170-2176, 2005.

[45] F. Sharipov, and D. Kalempa, “Velocity slip and temperature jump coefficients for gaseous mixtures. II. Thermal slip coefficient,” *Physics of Fluids,* vol. 16, no. 3, pp. 759-764, 2004.

[46] R. A. Millikan, “Coefficients of Slip in Gases and the Law of Reflection of Molecules from the Surfaces of Solids and Liquids,” *Physical Review,* vol. 21, no. 3, pp. 217-238, 1923.

[47] V. S. Smoluchowski, “Ueber Wärmeleitung in Verdünnten Gasen,” *Annalen der Physik,* vol. 300, no. 1, pp. 101-130, 1898.

[48] G. Karniadakis, A. Beskok, and N. Aluru, *Microflows and Nanoflows: Fundamentals and Simulation*: Springer, 2005.

[49] T. D. Holman, “Numerical Investigation of the Effects of Continuum Breakdown on Hypersonic Vehicle Surface Properties,” PhD Thesis, University of Michigan, 2010.

[50] C. Cercignani, *Mathematical methods in kinetic theory*: Springer, 1969.

[51] R. S. Myong, “Gaseous slip models based on the Langmuir adsorption isotherm,” *Physics of fluids,* vol. 16, no. 1, pp. 104-117, 2004.

[52] N. T. P. Le, C. J. Greenshields, and J. M. Reese, ”Evaluation of nonequilibrium boundary conditions for hypersonic rarefied gas flows. ” *EUCASS Proceedings Series, vol. 3,* pp. 217-230, 2012.

[53] F. Sharipov, and V. Seleznev, “Data on Internal Rarefied Gas Flows,” *Journal of Physical and Chemical Reference Data,* vol. 27, no. 3, pp. 657-706, 1998.

[54] D. R. Emerson, X.-J. Gu, S. K. Stefanov *et al.*, “Nonplanar oscillatory shear flow: From the continuum to the free-molecular regime,” *Physics of Fluids,* vol. 19, no. 10, pp. 107105, 2007.

[55] S. Albertoni, C. Cercignani, and L. Gotusso, “Numerical Evaluation of the Slip Coefficient,” *Physics of Fluids,* vol. 6, no. 7, pp. 993-996, 1963.

[56] T. Schwartzentruber, and I. D. Boyd, “Investigation of Continuum Breakdown in Hypersonic Flows Using a Hybrid DSMC-NS Algorithm,” *40th Thermophysics Conference*, Fluid Dynamics and Co-located Conferences: American Institute of Aeronautics and Astronautics, 2008.

[57] T. A. Oliver, “A High-Order, Adaptive, Discontinuous Galerkin Finite Element Method for the Reynolds-Averaged Navier-Stokes Equations,” PhD Thesis, Massachusetts Institute of Technology, 2008.

[58] K. J. Fidkowski, “A High-Order Discontinuous Galerkin Multigrid Solver for Aerodynamic Applications,” Master Thesis, Massachusetts Institute of Technology, 2004.

[59] J. F. Padilla, and I. D. Boyd, “Assessment of gas-surface interaction models for computation of rarefied hypersonic flow,” *Journal of Thermophysics and Heat Transfer,* vol. 23, no. 1, pp. 96-105, 2009.

[60] S. Dietrich, and I. D. Boyd, “Scalar and parallel optimized implementation of the direct simulation Monte Carlo method,” *Journal of Computational Physics,* vol. 126, no. 2, pp. 328-342, 1996.